Neoproterozoic magmatic accretion and Pan-African reworking-differentiation of mafic crust derived from an enriched mantle: evidences from structural analysis, petrology and geochemistry of the Ketté gold district (Eastern Cameroun)

Accrétion magmatique Néoprotérozoïque et remobilisation-différenciation d'une croûte mafique dérivée du manteau enrichi: évidences issues de l'analyse structurale, de la pétrologie et de la géochimie des formations du district aurifère de Ketté (Est Cameroun)

Ghislain Ngassam Mbianya[a,b,*], Olivier Vanderhaeghe[b], Sylvestre Ganno[c], Michel Gregoire[b], Mathieu Benoit[b], Rodolph Loïque Azefack Mbounou[a,d], Jonas Didero Takodjou Wambo[e], Timoleon Ngnotue[a]

[a] Department of Earth Sciences, University of Dschang, P.O. Box. 67, Dschang, Cameroon
[b] GET, Université de Toulouse, CNRS, CNES, IRD, UPS, Toulouse, France
[c] Department of Earth Sciences, University of Yaounde I, P.O. Box. 812, Yaounde, Cameroon
[d] Géosciences Montpellier, Université de Montpellier, CNRS-UMR 5243, Place E. Bataillon, Montpellier 34095, France
[e] Department of Earth and Space Sciences, Lamar University, Beaumont, TX 77705, USA

*Corresponding author: mbianya97@gmail.com (Ghislain Ngassam Mbianya)

Highlights

- Metapyroxenite and amphibolite of the Ketté district attest for magmatic accretion of a Neoproterozoic crust.
- Geochemical signatures of metapyroxenite and amphibolite of the Ketté district point to a pre-Neoproterozoic enriched mantle beneath the Central African Orogenic Belt.
- Migmatite, heterogeneous granite, tonalite, and granodiorite of the Kette district result from reworking of the mafic juvenile crust and associated sediments.
- The structural record of the Ketté district attests for syntectonic partial melting and differentiation of the root of the Central African Orogenic Belt.

Abstract

The gold-rich Ketté formations belong to the Adamawa-Yadé block of the Neoproterozoic Central Africa Orogenic Belt. They consist of a complex association of tonalite, granodiorite, and heterogeneous granite including rafts of metapyroxenite, amphibolite, paragneiss and migmatite. Metapyroxenite and amphibolite are metaluminous (A/CNK: 0.65-0.95), calc-alkaline, enriched in LILE and LREE, with $\varepsilon Nd_{610} < 0$ and T_{DM} ages of 1.7 Ga, highlighting their enriched mantle source. Paragneiss are rich in LREE, Cr, V, Sc and Ni and display A/CNK (1.06-1.08) and A/NK (1.5-3.49) ratios consistent with a sedimentary protolith made of poorly sorted greywackes and litharenites with a contribution from mafic rocks of the juvenile crust.

Granitoids display a variety of signatures, ranging from metaluminous to peraluminous (A/CNK: 0.94-1.04), calc-alkaline to alkaline. The heterogeneous granite in diffuse contact with migmatite have εNd_{654} values of –9.61 and –8.11, and are interpreted to reflect local magma collection within the zone of dominant partial melting of the paragneiss. The tonalite and granodiorite, characterized by magmatic textures, display Mg# of 39.9–48.8, low HFSE contents, and enrichment in LILE and LREE. They were likely formed by the fractional crystallisation of a dioritic magma derived from the partial melting of amphibolite.

The main structure of the migmatite is a shallow- to moderately dipping NE–SW trending syn-migmatitic foliation S_{mgm}, marked by alternating leucosome and mesosome layers, with relics of an S_0/S_1 foliation locally preserved within the mesosome. Granulite-facies relics with a peak at 8-10 kbar/≥800 °C are preserved in metapyroxenite. Networks of texturally continuous leucosome veins concordant to discordant to the syn-migmatitic foliation, localization of granitic veins in shear zones and fold axial planes, attest for deformation in the presence of melt. Granitoids form kilometre-scale plutons with gently dipping magmatic fabrics (S_m-S_m/C_2) concordant to the syn-migmatitic foliation. These fabrics are transposed into a steeply dipping (47°-74°) E–W to NW–SE trending mylonitic fabric (S_{myl}-S_3/C_3), bearing a moderately plunging (15°-49°) stretching lineation L_3, marking the folded Mama Shear Zone (MaSZ).

These data indicate that the Ketté region has recorded magmatic accretion of a mafic crust originating from an enriched mantle source. This crust and its associated sediments were subsequently tectonically thickened during the Pan-African orogeny and affected by partial melting. Migration of dioritic to granitic magmas from the partially molten orogenic root led to syntectonic crustal differentiation.

Keywords: Pan-African orogeny; Eastern Cameroon; enriched mantle; partial melting; crust-derived melts; migmatite.

Résumé

Les formations aurifères de Ketté, dans le bloc Adamawa-Yadé de la Ceinture Orogénique d'Afrique Centrale, sont constituées d'une association complexe de tonalite, granodiorite et granites hétérogènes, renfermant des enclaves de metapyroxénite, d'amphibolite, de paragneiss et de migmatite. Les metapyroxénites et amphibolites sont métalumineuses, enrichies en LILE et LREE, avec des valeurs $\varepsilon Nd_{610} < 0$ et des âges modèles T_{DM} de 1.7 Ga, indiquant une source mantellique enrichie. Les paragneiss sont riches en LREE, Cr, Sc et Ni et présentent des rapports A/CNK et A/NK caractéristiques de protolithes riches en greywackes et litharénites, avec une contribution de roches mafiques issues de la croûte juvénile.

Les granitoïdes ont des signatures métalumineuses à peralumineuses, calco-alcalines à alcalines. Les granites hétérogènes présentent des contacts diffus avec les migmatites, des valeurs εNd_{654} de -9.61 et -8.11, et reflètent une accumulation locale de magma au sein de zones de fusion partielle dominante des paragneiss. Les tonalites et granodiorites présentent des textures magmatiques, des valeurs Mg# de 39.9-48.8, de faibles teneurs en HFSE et des enrichissements en LILE et LREE. Elles résulteraient de la cristallisation fractionnée d'un magma dioritique issu de la fusion partielle des amphibolites.

Les migmatites présentent une foliation syn-migmatitique S_{mgm} orientée NE-SW, à pendage faible à modéré, marquée par l'alternance leucosomes-mésosomes, avec des reliques de la foliation S_0/S_1 localement préservées. Des reliques du faciès granulitique témoin d'un pic métamorphique à 8-10 kbar/≥800 °C sont conservées dans les metapyroxénites. Les réseaux continus de leucosome, concordants à discordants à la foliation syn-migmatitique, ainsi que la localisation des veines granitiques dans des zones de cisaillement et dans les axes des plis, témoignent d'une déformation en présence de magma. Les plutons kilométriques de granitoïdes présentent des fabriques magmatiques (S_m-S_m/C_2) à faible pendage, concordantes avec la foliation syn-migmatitique. Ces fabriques sont transposées en des fabriques mylonitiques (S_{myl}-S_3/C_3) orientées E-W à NW-SE à fort pendage (47°–74°), portant une linéation d'étirement Le_3 à plongement modéré (15°–49°), dans la zone de cisaillement plissée de Mama.

Ces données indiquent que le socle de Ketté a enregistré l'accrétion d'une croute mafique dérivée de la fusion du manteau enrichi. Cette croûte et les sédiments y associés ont ensuite été tectoniquement épaissis durant l'orogénèse Pan-Africaine, favorisant la fusion partielle. La migration de magmas de composition dioritique à granitique issus de la racine orogénique partiellement fondue a conduit à une différenciation crustale syntectonique.

Mots-clés: Orogénèse Pan-Africaine; Est Cameroun; manteau enrichi; fusion partielle; magma crustal; migmatites.

1. Introduction

The Central African Orogenic Belt (CAfOB) runs across Cameroon, Nigeria, Chad, the Central African Republic, and Sudan (Nzenti et al., 1988; Van Schmus et al., 2008). It was formed during the Neoproterozoic Pan-African orogeny and contributed to the amalgamation of western Gondwana (Kröner and Stern, 2004). The significance of Archean, Paleoproterozoic, Mesoproterozoic and early Neoproterozoic geochronological inheritances preserved in metamorphic and magmatic rocks is debated (Tanko Njiosseu et al., 2005; Liégeois et al., 2013; Ganwa et al., 2016; Tchakounté et al., 2017; Saha-Fouotsa et al., 2019; Djerossem et al. 2020). They could reflect the nature of the mantle source of Neoproterozoic magmas, and/or tectonic reworking of a variety of pre-Pan-African crustal domains and/or of sediments derived from these pre-Pan-African crustal domains. Accordingly, the CAfOB provides an excellent target to characterize the processes of crustal growth and differentiation, and their relationship with orogeny during the Precambrian era. Furthermore, in Cameroon, the CAfOB is known for its numerous orogenic gold deposits and uranium mineralization related to shear zones and associated hydrothermalism (Azeuda et al., 2022; Ngounouno et al., 2022; Ngassam Mbianya et al., 2021; Kouske et al., 2022; Takodjou Wambo et al., 2024), as well as iron (Motto Mbita et al., 2024) and Zr-REE-Y mineralization (Tchoupe et al., 2024). Understanding the tectonic, metamorphic and magmatic evolution of the CAfOB is thus crucial for future exploration of these ore deposits.

In Cameroon, a new geological synthesis has been provided by the PRECASEM mapping project (Delor et al., 2021). Nevertheless, the nature of the orogenic crust and the processes leading to the formation of the CAfOB are still a matter of debate. For instance, in the Adamawa-Yadé block (AYB) or central Cameroon domain, some authors (e.g. Toteu et al., 2022; Shellnutt et al., 2017; Abdelsalam et al., 2002; Liégeois et al., 2013) favour a model of collision between the Archean and Paleoproterozoic West African, Congo, São Francisco

Cratons and the enigmatic Sahara Metacraton. Other authors support the idea of a collision between microcontinents of Paleoproterozoic age and magmatic arcs of Neoproterozoic age formed along the edge of the Congo Craton (Bouyo Houketchang et al., 2009, 2015; Toteu et al., 2004; Tchakounté et al., 2017). In contrast, Saha-Fouotsa et al. (2019) in Central Cameroon and Djerossem et al. (2020) in the Ouaddai massif, argue that Archean and Paleoproterozoic zircon cores of migmatitic gneiss are detrital and their U-Pb dates thus trace the source of the sediments reworked during the Pan-African orogeny rather than the age of reworked crustal blocks. On the other hand, several studies document the nature of mantle-derived magmatic rocks and their contribution to Neoproterozoic crustal growth (Kwékam et al., 2010; Tchouankoue et al., 2016; Fuh et al., 2021; Ayonta Kenné et al., 2023). Diorite and quartz-monzodiorite from Fomopéa contain zircon grains that yield U–Pb ages of 620 ± 3 Ma and 613 ± 2 Ma. The $\varepsilon_{Nd(620\ Ma)}$ values range from +4 to –16, with T_{DM} model ages between 0.9 and 2.9 Ga, suggesting an origin involving mixing between mantle-derived melts and Palaeoproterozoic to Archaean lower continental crust (Kwékam et al., 2010). Shoshonitic syeno-monzonite of Bangangte enriched in LILE and LREE, with $\varepsilon_{Hf}(t) < 0$ and a zircon U-Pb age of ca. 584 Ma, are interpreted to have originated from partial melting of an enriched mantle source, with varying degrees of crustal contamination (Tchouankoué et al., 2016). High-K, metaluminous and alkaline to sub-alkaline syenite and mafic microgranular enclaves of Linte, with U–Pb zircon ages of 599 ± 3 Ma and 597 ± 4 Ma, are interpreted to have formed from a mantle-derived magma with a significant crustal contribution (Ayonta Kenné et al., 2023). While the geochemical signatures of mafic rocks most likely reflect the nature of the mantle source, the interpretation of those of intermediate to felsic magmatic rocks is more complex. These rocks may have formed either through the fractional crystallisation of mantle-derived magmas or through the partial melting of mafic rocks, with varying contributions from metasediments.

In addition to the growth and magmatic history, the tectonic evolution of the CAfOB in Cameroon remains topical. Most studies do not provide detailed structural analysis and rely primarily on geochemical and/or geochronological data to establish evolutionary models. The role of major shear zones and faults in the generation, migration, and emplacement of magma remains poorly constrained. Some studies have documented relationships between magma emplacement and the activity of the Central Cameroon Shear Zone and the Tcholliré–Banyo Shear Zone (e.g. Kwékam et al., 2010; Nomo Negué et al., 2017). In contrast, the Sanaga Fault in eastern Cameroun, which is also represented as a major structure, and its associated satellite shear zones have been poorly investigated, except for detailed structural analysis in Bétaré-Oya (Kankeu et al. 2009) and in Guiwa-Yangamo (Nomo-Negué et al., 2021). Does it correspond to a suture zone localizing the deposition-emplacement of the protoliths of greenstones of the so-called Lom basin and/or a post-collision shear zone? Moreover, what is the relationship between magma generation and emplacement, and the activity of the Sanaga Fault and its satellite structures?

In this paper we document the petrological, structural and geochemical record of the magmatic and metamorphic rocks in the Ketté gold district, located south of the Sanaga Fault and along the border with the Central African Republic, with emphasis on the Mama Shear Zone (MaSZ). The study aims to constrain the crustal and tectonic evolution of the Ketté district. Furthermore, the data presented allow us to discuss (i) the source of the protoliths of the amphibolite, metapyroxenite and paragneiss; (ii) their relationships with migmatite and granitoids and their significance for crustal differentiation; and (iii) the tectonic implications of their structural record. The structural data provide field-scale evidence for the evolution of amphibolites and paragneisses into partially molten rocks and subsequently into granitoids through partial melting, melt segregation and migration, and magmatic differentiation. They also constrain the syn-tectonic emplacement of the granitoids and their subsequent post-

magmatic deformation. These observations provide new petrogenetic insights and allow a more robust identification of the source rocks of the granitoids. They further establish a structural and tectonic framework that will serve as a basis for future research and mineral exploration in the Eastern Cameroon gold district.

2. Geological setting

2.1. Geology of the CAfOB

The CAfOB, also known as the Pan-African North Equatorial Fold Belt or the Central African Fold Belt, comprises three different domains in Cameroon: (Nzenti et al., 1988; Ngnotue et al., 2000; Toteu et al., 2022; Fig. 1a):

(1) The west Cameroon domain extends from the northwest of the Tcholliré-Banyo Shear Zone (TBSZ) to the Mayo-Kebbi domain in Chad (Penaye et al., 2006). It comprises metavolcanics and metavolcanosediments of the Poli Group and the Rey-Bouba greenstone belt, whose protolith is dated at ca. 830 Ma and ca. 670 Ma (Toteu et al., 2006; Bouyo Houketchang et al., 2009). It also includes pre-, syn- to late-tectonic calc-alkaline granite emplaced between 660 and 580 Ma (Kwékam et al., 2010; Dawaï et al., 2013). In addition, post-tectonic alkaline granitoids are present, with U-Pb zircon ages of ca. 567 Ma (Isseini et al., 2012).

(2) The central domain or Adamawa-Yadé block (AYB) is limited to the North by the Tcholliré-Banyo shear zone (TBSZ) to the south of the Sanaga fault, and includes the Central Cameroon shear zone (CCSZ). It is a composite domain dominated by granite-gneissic complexes with Archean to Paleoproterozoic inheritances (Tchakounté et al., 2017; Ganwa et al., 2016), as well as greenstone belts interpreted as former volcanosedimentary basins (Soba et al., 1991; Toteu et al., 2006) and some juvenile Neoproterozoic plutonic rocks (Kwékam et al., 2010; Saha-Fouotsa et al., 2019; Fuh et al., 2021; Ayonta Kenne et al., 2023). Neoproterozoic Pan-African magmatism is syn- to post-collisional, calc-alkaline to alkaline, and emplacement of plutons is

localized along major shear zones/faults (Nzenti et al., 2006; Hamdja Ngoniri et al., 2021; Kamguia Kamani et al., 2021). The granitoids are hosted by high-grade ortho- and para-gneiss with Archean, Paleoproterozoic and Neoproterozoic protoliths (Tanko Njiosseu et al., 2005; Nzenti et al., 2006; Ganwa et al., 2008). Four deformation phases are currently recognised (Kankeu et al., 2009; Nomo Negue et al., 2021; Azefack Mbounou et al., 2026). Gold mineralisation is found within the Eastern Cameroon district (Suh et al., 2006).

(3) The southern domain or Yaoundé-Yangana nappes comprise a set of metasedimentary series including the Yaoundé group, the Yangana group, and the Mbalmayo-Ayos-Bengbi group. It consists of medium to high-grade rocks derived from mixed protolith of Neoarchean-Paloproterozoic-Neoproterozoic age, metamorphosed between 630 and 580 Ma (Penaye et al., 1993; Toteu et al., 2006; Nkoumbou et al., 2014). Plutonism occurs between 830 and 620 Ma (Owona et al., 2011; Toteu et al., 2022).

The NNE-SSW trending sinistral TBSZ has been proposed to represent a major boundary between the juvenile crust of the West Cameroon Domain (WCD) and the AYB dominated by reworking of a pre-Panafrican continental crust (Toteu et al., 2004; Ngako et al., 2008; Nomo Negué et al., 2017). The CAfOB is also crosscut by a series of regional shear zones including the dextral CCSZ (Ngako et al., 2008; Saha-Fouotsa et al., 2019) and the Sanaga Fault (SF) with uncertain kinematics that marks the contact between the Lom series and high-gradegneiss and plutonic rocks (Soba et al., 1991; Kankeu et al., 2009; Ngako et al., 2003). In eastern Cameroon, the SF ends in Central African Republic where it is known locally as the Bozoum-N'délé shear zone (Topien et al., 2023; Djamous et al., 2026).

2.2. Geological setting of the Eastern Cameroun gold district

The eastern Cameroon gold district comprises the Bétaré-Oya, Batouri, Ketté and Boden sub-districts (Fig. 1b). Bétaré-Oya comprises the Lom meta-volcanosedimentary series and I-

Type syntectonic granite with calc-alkaline affinity dated between 650 and 620 Ma, with $\varepsilon_{Hf}(t)$ (-13.80 to -6.20) interpreted as reflecting a crustal origin (Azeuda et al., 2022). Zircon U-Pb geochronology on the metasediments points to the contribution of Archean (~2500 Ma), Mesoproterozoic (~1100 Ma), and Neoproterozoic (~735 Ma) sources in the sedimentary protoliths and document high-temperature metamorphism between 665-585 Ma (Soba et al., 1991; Toteu et al., 2004, 2006; Azeuda et al., 2022). The Batouri sub-district exposes sub-alkaline I-Type granodiorite, granite, and tonalite emplaced between 624 and 589 Ma (U-Pb on zircon and Ar-Ar on K-feldspar and whole rock; Asaah et al., 2015). The Ngoura, Colomines, Ouaden, and Doumba Bello sub-districts consist of gabbro, granodiorite, and granite. Granite and granodiorite are calc-alkaline to shoshonitic, with U-Pb ages on zircon of 640 - 638 Ma, $\varepsilon_{Nd}(t)$ (-9.6 to -6.3), and $\varepsilon_{Hf}(t)$ (-10.1 to -2.1) pointing a crustal origin (Ngatcha et al., 2019; Lemdjou et al., 2022). A U-Pb/zircon age of 641 ± 4 Ma and $\varepsilon_{Hf}(t)$ values of -12.72 and -6.46 have been obtained on a biotite granite from Béké, Ketté (Azeuda et al., 2022). Rocks of the Eastern Cameroon district are crosscut by a network of NE-SW, E-W, and NW-SE trending shear/fault zones controlling the distribution of lode gold mineralization, accompanied by a variety of wall-rock alterations (Tata et al., 2018; Vishiti et al., 2018; Takodjou Wambo et al., 2024).

3. Methodology

3.1. Sampling and structural analysis

The study area was divided into six zones to facilitate the planning of the exploration campaigns. Hammer prospecting, based on the search for outcrops, was employed due to the thick lateritic cover. At the various sites surveyed, the types of outcrops and the colour of the rock were recorded. The structural features were carefully identified, described and measured. A preliminary relative deformation chronology was established in situ. Photographs were then taken at regular intervals, taking into account geometric parameters. Finally, samples were carefully collected from all the different petrographic types identified. In total, four samples of

metapyroxenite, nine samples of amphibolite, eight samples of paragneiss, twenty samples of migmatitic gneiss, forty-five samples of granitoids, and twenty-five samples of mylonitised granitoids were collected. The structures were plotted on lower-hemisphere Schmidt diagrams using Stereonet v.8 software. Forty-three thin sections and polished thin sections were made at the Langfang Rock Detection Technology Service Limited and the Géosciences Environnement Toulouse (GET) laboratory.

3.2. Whole-rock geochemistry

The samples selected for analysis were chosen to cover all the different petrographic types identified. Representative samples were ground, crushed, and pulverised using an agate mortar at GET (France). Major and trace element concentrations were measured at the SARM of the CRPG in Nancy (France), following the protocol of Carignan et al. (2001). The powders were fused with lithium metaborate ($LiBO_2$) at ~980 °C. The resulting glass were dissolved in a nitric acid solution ($HNO_3 \pm H_2O_2$ and glycerol). Analyses of major elements (including Sc) were conducted by ICP-OES using a Thermo Fisher iCAP 6500 spectrometer. Trace elements were analysed by ICP-MS using a Thermo Fisher iCAP Q spectrometer. Calibration was performed using international geostandards and analytical accuracy was monitored through repeated measurements of reference materials and blanks. Detection limits are detailed in Supplementary Tables S1, S2.

3.3. Sr-Nd isotopes

Sr and Nd isotopic analyses were carried out at the CRPG (Nancy, France). Between 100 and 200 mg of powdered samples were dissolved in HF-HNO_3-$HClO_4$ mixtures at 110-120 °C for 24 h. Before complete evaporation, the residues were treated with concentrated HNO_3 to eliminate fluorides and then redissolved in HCl. Sr, Sm, and Nd were separated by column chromatography following the procedure of Luais et al. (1997). Sm and Nd isotopic ratios were determined using a MC-ICP-MS (Isoprobe, Micromass), whereas Rb isotopic compositions

were analysed by ICP-MS (PerkinElmer ELAN 6000). Strontium isotopic ratios were measured using a TIMS (Finnigan). During the analytical session, the measured value for the NBS 987 standard was $^{87}Sr/^{86}Sr = 0.710253 \pm 0.000009$, and the JMC standard yielded a $^{143}Nd/^{144}Nd$ ratio of 0.512231 ± 0.000070. The external reproducibility of the Isoprobe instrument is estimated at ±0.000030 for the measured isotopic ratios.

4. Results

4.1. Lithological units (petrography, structure and microstructure)

The Ketté area (Fig. 2) is dominated by a heterogeneous granite in diffuse contact with migmatite and containing lenses and rafts of amphibolite, metapyroxenite, schists and paragneiss; and intruded by more homogeneous tonalite and granodiorite (Fig. 3a, 3c, 3e, 3i, 3j). To the south of the studied area, the E-W to NW-SE (N95-130°E) trending Mama Shear Zone (MaSZ) crosscuts all lithological units and is marked by a protomylonitic to ultramylonitic fabric.

4.1.1. Ultramafic and mafic rocks

Ultramafic and mafic rocks are generally structurally and texturally associated in the field and are present as boudinaged layers and/or enclaves (Figs. 3a, 3b) aligned in the foliation of heterogeneous granitoids, tonalite and granodiorite. Only the larger ones (more than 100 m wide) are represented on the map of figure 2.

Metapyroxenite have a heterogranular granoblastic microstructure (Fig. 3d). The primary Opx+Cpx+Pl paragenesis is characteristic of metamorphic conditions of ~800°C/8-10 Kbar (Burcher and Grapes, 2011). These pressure-temperature conditions correspond to the metamorphic peak and provide the first evidence of granulite facies in the Eastern district.

Apatite is the main accessory mineral. Pyroxene prisms are partially retrogressed into amphibole and biotite.

Amphibolite have a grano-mematoblastic microstructure. The paragenesis consists of Amp+Pl+Kfs+Qtz+Bt, which is characteristic of the middle amphibolite facies at 4–5 kbar/550–600 °C (Bucher and Grapes, 2011). Hornblende occurs as poikilitic, locally acicular subhedral to anhedral prisms in a matrix of plagioclase and K-feldspar with interstitial quartz (Fig. 3e). The preferred orientation of amphiboles delineates an S_n foliation that is wrapped by the S_{mgm} syn-migmatitic foliation (Fig. 3b).

4.1.2. Paragneiss

Paragneiss are generally structurally associated with amphibolite (Figs. 3b, 3c). Paragneiss display a composite $S_{0/n}$ foliation marked by the alternation of layers of coarse quartz and feldspar grains with layers rich in biotite and/or amphibole, and/or pyroxene (Fig. 3c).

Amphibole and pyroxene paragneiss exhibit a heterogranular oriented granoblastic microstructure. Orthopyroxene (hypersthene) is retrogressed into hornblende and biotite. Clinopyroxene (augite) occurs as small prisms surrounded by a reaction rim at the contact of orthopyroxene and hornblende prisms (Fig. 3f). Hornblende is retrogressed into biotite, muscovite, and talc.

Biotite and amphibole paragneiss (Fig. 3c) display an oriented granolepidoblastic microstructure. Biotite lamellae mould the phenoclasts (Fig. 3g). The plagioclase phenoclasts are poikilitic and locally antipertithic (Fig. 3g). The paragenesis consists of Hbl+Pl+Kfs+Qtz+Bt and is characteristic of the amphibolite facies at ~500±50 °C. Retrograde transformations are related to the retromorphosis of amphiboles into biotite and chlorite [Hbl+Pl+H_2O → Qtz+Bt+(Op), Hbl+Pl+H_2O → Qtz+Chl+(Op)] (Tcheumenak Kouémo et al., 2023; Burcher and Grapes, 2011).

316 **4.1.3. Migmatite**

317 Migmatite of amphibolite and paragneiss (Figs. 3b, 3c) are typically metatexite
318 characterized by a S_{mgm} syn-migmatitic foliation (Fig. 4a) defined by the alternation of the
319 leucosome-melanosome-mesosome triplet. The mesosome exhibits an heterogranular
320 granoblastic microstructure, with a layered arrangement of quartz and feldspars alternating with
321 biotite-rich levels (Fig. 4b). The quartz-feldspar leucosome displays interlocked texture with a
322 variable grain size and forms a texturally continuous network of veins concordant to discordant
323 relative to the synmigmatitic foliation (Fig. 4c). The paragenesis are Qtz+Kfs+Pl+Bt+Amp and
324 Qtz+Kfs+Pl+Bt characteristic of amphibolite facies. Pyroxene is retrogressed into biotite and
325 amphibole and amphibole is retrogressed into biotite (Opx + Kfs + H_2O → Bt + Qtz + Op, Opx
326 + Pl + Qtz + H_2O → Amp + Pl) attesting for rehydration (Tcheumenak Kouémo et al., 2023).

327 **4.1.4. Granitoids**

328 ***Tonalite***

329 Tonalite and granodiorite do not form individual plutons but correspond to different
330 facies identified in the studied area. The porphyritic tonalite (Fig. 5a) consists of plagioclase (~
331 48 %) and K-feldspar (~ 4 %) subhedral to anhedral phenocrysts with interstitial quartz (~ 21
332 %) biotite (~ 17 %), hornblende (~ 5 %) and clinopyroxene (~ 3 %). Plagioclase, K-feldspar
333 and hornblende are locally stretched/elongated. Quartz is recrystallized into polygonal grains
334 indicative of grain boundary migration recrystallisation (GBM) at 500-700 °C (Stipp et al.
335 2002b; Bons and Urai, 1992). Myrmekitic and perthitic textures (Fig. 5d) are common.
336 Accessory minerals (~ 2 %) are titanite, apatite, zircon and opaques.

337 ***Granodiorite***

The porphyritic granodiorite is characterized by subhedral feldspar megacrysts with rounded corners. They contain plagioclase (~ 39 %), quartz (~ 25 %), biotite (~ 20 %), K-feldspar (~ 9 %), hornblende (~ 4 %) and clinopyroxene (~ 2 %). Accessory minerals (~ 1 %) are zircon, monazite, fluorapatite and Fe-oxides.

Heterogeneous granite (diatexite)

Metatexite grade into diatexite made up of heterogeneous granite (Figs. 4c, 4d). The granite and alkali feldspar granite are distinguished based on their relative proportions of alkali feldspar and plagioclase in the modal QAPF diagram of Streckeisen. Medium- to coarse-grained **granite** is pink to light grey and contains K-feldspar (32-42%), quartz (19-36%), biotite (15-25%), plagioclase (13-16%) and amphibole (4-7%). Accessory minerals (~ 3 %) are pyrite, magnetite, titanite, zircon and monazite. The medium-grained **alkali feldspar granite** consists of subhedral K-feldspar (44-48%), quartz (22-26%), biotite (16-20%), plagioclase (4-6%) and amphibole (3-5%). Biotite flakes are grouped into clusters. Accessory minerals (~ 3 %) are zircon, pyrite, apatite and magnetite.

The S_m magmatic foliation in the granitoids is defined by the preferred orientation of coarse-grained feldspar (Figs. 4d, 5a, 5b, 5e), it is also marked by the preferential orientation of the biotite schlierens. Fractures in plagioclase grains indicate deformation under melt-present conditions (Fig. 5g). The filling of fractures suggests the involvement of a silicate melt and high temperatures above 650 °C (Bouchez et al., 1992; Fazio et al., 2020). The granitoids locally show evidence of intracrystalline solid-state deformation and display S/C fabrics, with sigmoid-shaped grains (Fig. 5c). The schistosity is underlined by the shape preferred orientation (spo) of crystals (Fig. 5f) and by the recrystallization of quartz and feldspar into subgrains. The quartz grains show undulatory extinction, indicative of plastic deformation mechanisms operating at 300-450 °C (Passchier and Trouw, 2005). The σ- and δ- porphyroclasts (Fig. 5c) of feldspar is

indicative of non-coaxial deformation. Deformed polysynthetic twins suggest low temperatures or low strain (Blenkinsop, 2002). These features are indicative of a deformation continuum from magmatic to solid state (Passchier and Trouw, 2005; Blenkinsop, 2002).

4.1.5. The mylonitic Mama Shear Zone

The MaSZ is characterised by the transposition of the magmatic/submagmatic fabric of granitoids into a mylonitic to ultramylonitic fabric, marked by the development of a mineral stretching lineation L_{n+2} and mylonitic foliation planes S_{myl} (Fig. 6a, 6b), resulting from dynamic recrystallization expressed by a variety of microstructures. The S_{myl} ultramylonitic foliation is related to a layered arrangement of fine-grained quartz and feldspar alternating with biotite- and amphibole-rich layers (Fig. 6b). In protomylonite and mylonite, a penetrative foliation S_{myl} is defined by discontinuous ribbons of quartz-feldspars and/or biotite-magnetite intersected by C_{n+2} shear planes. These ribbons are included in a relatively fine feldspar-rich matrix; outlining a grain shape preferred orientation (gspo), and S_{myl}/C_{n+2} composite structures (Fig. 6a, 6c). Lobate and amoeboid quartz grains (Fig. 6d, 6e, 6f) are dispersed into quartz with straight grain boundaries at 120° defining a subpolygonal texture (Fig. 6g) that indicate grain boundary migration recrystallisation (GBM) at 500-700 °C (Stipp et al. 2002b; Bons and Urai, 1992). The folded ribbons of feldspar subgrains, σ-sigmoids (fig. 6e), asymmetric feldspar grains, the obliquity of C_{n+2} shear planes relative to S_{myl} foliation planes (Fig. 6c), and biotite fish point to a dominant dextral movement. The Φ-sigmoids of feldspars (fig. 6c) testify to a part of coaxial deformation. Subgrains and recrystallised grains surround phenoclasts, defining core-mantle structures (Fig. 6h) in ultramylonite, indicative of intermediate-temperature conditions (Hirth and Tullis, 1992; Passchier and Trouw, 2005). Biotite and amphibole are sigmoidal. Kinematic indicators at this stage include δ and ovoid phenoclasts. In protomylonite, bulges at the margins of feldspar and quartz grains indicate bulging recrystallisation (BLG),

occurring around 280–400 °C (Stipp et al., 2002b; Bons and Urai, 1992). Similar bulges are also observed in some tonalite (Fig. 5d). Quartz grains exhibit undulatory extinction.

4.2. Regional scale structural pattern

4.2.1. Structures of ultramafic and mafic rocks, and paragneiss

The $S_{0/n}$ and S_n foliations preserved in paragneiss and amphibolite are attributed to a D_1 deformation phase. These structures are wrapped into the syn-migmatitic foliation (Figs. 3b, 3c 7a). Accordingly, their current orientation is most probably not representative of their original position at the time of deformation, but reflects their transposition in the presence of melt.

4.2.2. Structures of migmatite

The syn-migmatitic foliation S_{mgm} of the metatexite (Fig. 4a) displays NE–SW to E–W orientations, with low to moderate dips (21°-67°) towards the NW and SE (Fig. 8a). Concordant leucosome veins are in textural continuity with discordant leucosome localized in boudins necks and shear zone (Fig. 7a). Leucosome veins are affected by isoclinal folds with axial planes parallel to the syn-migmatitic foliation and an axis plunging to the NE (Fig. 7b).

The syn-migmatitic foliation is crosscut by syn-migmatitic C_{mgm} shear planes leading to the formation of pinch and swell boudins (Fig. 7c), C_{mgm} sinistral strike-slip faults (Fig. 7d), granitic injection-related dextral shear planes (Fig. 7e), and C_{mgm} strike-slip faults (Fig. 7f) oriented N84°E/25°W and N130°E/40°NE. Asymmetrically folded leucosomes F_{n+1}, consistent with a dextral sense of shear (Figs. 7g, 7h), have an axial plane oriented N80–84°E/28°W and N39°E/24°SW (Fig. 8b). Different generations of syn-migmatitic folds produce interferences patterns (Fig. 7d) corresponding to viscous folds (McLellan, 1984). Crenulation cleavage with sinistral shear planes oriented N70°E/30NW and dextral shear planes oriented N123°E/38NE is observed in the metatexite (Fig. 7i) and diatexite respectively.

409 **4.2.3. Structures of granitoids**

410 The S_m magmatic foliation displays a wide range of orientations, with low to moderate
411 (16°-33°) dips (Fig. 8c). The magmatic foliation is transposed into discrete sinistral C_{n+2} shear
412 planes oriented N170°E. Sinistral C_{n+2} strike-slip faults oriented N160°E result in the formation
413 of asymmetric boudins (Fig. 9a). The magmatic foliation S_m generally concordant with the syn-
414 migmatitic foliation S_{mgm}, together with the various syn-migmatitic and magmatic structures,
415 belongs to the progressive D_2 deformation phase. This phase developed under partially molten
416 conditions within shear zones accommodating ductile, non-coaxial deformation.

417 **4.2.4. The MaSZ pattern**

418 ***Mylonite***

419 The mylonitic S_{myl} foliation predominantly trends E-W with a moderate to steep (45°-
420 74°) dips (Fig. 8d). The dispersion of measurements is attributed to asymmetric folds affecting
421 the mylonitic fabric, observed at the outcrop scale and reconstructed at the regional scale. The
422 stretching lineation Le_{n+2} is related to quartz + feldspar +/- biotite +/- magnetite stretched grains
423 and trends E-W to WNW-ESE, with low to moderate (15°-49°) plunges (Fig. 8e). The narrow
424 ultramylonite bands rich in biotite are oriented ~N90°E. The development of mylonitic fabrics
425 is intimately linked to the development of shear planes C_{n+2} and second-order internal C_{n+3}
426 shears oriented N102°-N140°E to N160°-180°E, respectively. They thus define S/C composite
427 structures (see Figs. 6a, 6c).

428 ***Veins***

429 Some granitic veins are generally smoky, broken, thin (width: 1.5 - 15 cm) and have 30
430 cm to 2 m of length. They are generally arranged along the C_{n+3} shear planes, which induce
431 deflection of the S_{n+2} mylonitic foliation into S- and Z-shaped geometries (Figs. 9b, 9c). The

veins are generally parallel to the axial planes of F_{n+3} folds with an axial plane oriented E-W, N-S, NNE-SSW. These are interpreted as vein related-folds (Druguet, 2019). The F_{n+3} folds have low to moderate (13°-30°) plunges (Fig. 8d). Numerous folded quartz veins exhibit boudinage along their hinges (Fig. 9d). The straight to curved tension gashes, with long axes oriented N90°–100°E display crystalline growth fibres perpendicular to the walls with a dextral sense of shear (Fig. 9e).

Large scale folds

The mylonitic foliation in the MaSZ is affected by F_{n+2} isoclinal folds with an axial plane oriented N100-110°E/10-20°E (Fig. 9f). This induced the development of an km-scale (Fig. 9g) E-W to NW-SE (N91°E/40°S to N142°E/36°SE) trending F_{n+3} folds; with S- (Fig. 9h) and Z-shaped (Figs. 9i, 9j) second order folds on its normal and reverse limbs, oriented NE-SW to E-W with low (08°-20°) plunges (Fig. 8d). The axial plane of F_{n+3} M-folds is parallel to the C_{n+3} shear planes and exhibit a crenulation cleavage S_{n+3}//C_{n+3} (Fig. 9h). The various structures developed in the MaSZ belong to the D_3 deformation phase.

4.3. Whole rock geochemistry

4.3.1. Metapyroxenite and amphibolite

Major elements

Metapyroxenite and amphibolite are ultrabasic-basic to intermediate (SiO_2: 43.76-54.80%; Tab. 1). The samples display high content in MgO (5.19-7.36%), with Mg# [Mg# = 100*MgO/(FeO+MgO) molar] between 50.45 and 64.42. The FeO_t contents range from 6.70 to 12.86%, while the ferromagnesian contents (Fe_2O_3+MgO+MnO+TiO_2) range from 15.51 to 23.95%. Samples NGN5 and OUN2 are rich in Na_2O ($K_2O/Na_2O < 1$), while GN7 and NGN3 are rich in K_2O ($K_2O/Na_2O > 1$). In the MgO vs. Zr diagram (Geringer, 1979), the rocks plot in

455 the orthoderived field (Fig. 10a). They have basaltic to andesitic compositions (Winchester and
456 Floyd, 1977), belong to the calc-alkaline series (Figs. 10b, 10c) and are metaluminous (A/CNK
457 < 1).

458 ***REE and trace elements***

459 The investigated rocks are rich in LILEs (Ba: 104-2439 ppm; Rb: 91.9-238 ppm; Sr:
460 115-1259 ppm; Tab. 1) and show relatively low contents in Hf (3.50-4.15 ppm), Nb (4.83-12.0
461 ppm), and Ta (0.33-1.12 ppm). Zr (124-162 ppm) content is high. Transition metal contents are
462 high (Cr: 58.7-434 ppm; Ni: 23.6-136 ppm; Co: 30.7-50.1 ppm; Sc: 18.33-47.57 ppm).

463 Metapyroxenite and amphibolite samples display a steep slope in the primitive mantle-
464 normalized multi-elements diagram (Figure 11a), except for sample NGN5, which shows
465 negative anomalies in Ba and Sr. These anomalies may be explained by plagioclase
466 fractionation or could correspond to a melt residue separated from the plagioclase. The rocks
467 show negative anomalies in Th, Nb, Ta, Zr, and Ti while positive anomalies are common for
468 Ba, U, La, Nd and Sm. The rocks are enriched compared to MORB. Chondrite-normalized REE
469 patterns show higher HREE fractionation (Gd_N/Yb_N: 1.56-3.64) compared to LREE (Ce_N/Sm_N:
470 1.97 to 2.88), except for NGN5 (Fig. 11b). They display either negative Eu anomalies (Eu/Eu*
471 = 0.83-0.89) or either no anomaly (Eu/Eu* = 1.02). The $(La/Yb)_N$ ratio ranges from 8.59 to
472 18.80.

473 **4.3.2. Paragneiss and migmatitic gneiss**

474 ***Major elements***

475 Paragneiss and migmatitic paragneiss have SiO_2 contents ranging from 53.65% to
476 73.95% (Tab. 1) and high Al_2O_3 contents (10.01–18.22%). Their chemical index of alteration
477 (CIA) range from 60.48 to 77.66%, which is relatively low (Fig. 10g). Their Mg# varies
478 between 34.77 and 38.75. Their ferromagnesian (Fe_2O_3+MgO+MnO+TiO_2) content ranges

between 6.69% and 14.44%, while their CaO content ranges from 1.41% to 6.61%. Their K_2O/Na_2O ratios are 0.52-3.95. Their chemical compositions straddle the fields of shales, wackes, and litharenites on the Log (SiO_2/Al_2O_3) vs. Log (Fe_2O_3/K_2O) diagram of Herron (1988) (Fig. 11e) and is consistent with felsic to intermediate igneous and quartz-bearing sedimentary rocks (Fig. 10f).

REE and trace elements

The paragneiss and migmatitic gneiss display high contents in Rb (186-243 ppm), high to low content in Ba (1635-271 ppm) and Sr (777-161 ppm) compared to the UCC (Fig. 11c). HFSE contents (Hf: 4.34-10.5 ppm; Nb: 8.32-12.5 ppm, Ta: 0.12-1.0 ppm) are low, except for Zr (167-387 ppm). The U (2.24-3.74 ppm) and Th (10.8-13 ppm) contents are relatively similar to those of the UCC. The spider diagrams show relatively similar pattern (Fig. 11c) with positive anomalies in Rb, U, La, Pb, Nd, Zr, Dy and negative anomalies in Ba, Nb, Ce, Sr, and Ti. However, some samples (GN3, TN1, and TN2) are enriched in Cs, Rb, Ti, Zr and depleted in Ba, Rb, Nb, Ta, and K compared to the UCC. Migmatite sample GN3 is richer in U and Th than the other samples, as these incompatible elements preferentially concentrate in the leucosome during partial melting. In the chondrite-normalized REE diagrams (Fig. 11d), the rocks show negative Eu anomalies (Eu/Eu* = 0.30-0.82). GN3 has a positive Ce anomaly. The samples are enriched in LREE compared to HREE (La_N/Yb_N: 13.82-20.14; Gd_N/Yb_N: 2.48-5.67). The REEs sum is 101.38-243.24 ppm.

4.3.3. Granitoids

Major elements

Granitoids and their mylonitic and hydrothermally altered equivalents are presented together (Table 2). The mylonitised and/or altered rocks were investigated from both

petrographic and geochemical perspectives, revealing evidence of potassic and phyllic alteration. Element mobility associated with mylonitisation and/or weathering was further assessed using the isocon method, which indicates relative enrichments in LILE across the samples (Ngassam Mbianya, 2024). However, these alteration processes fall outside the main scope of the present study. In this manuscript, we ensure that all petrogenetic interpretations are not biased by these secondary modifications. Any observations deviating from expected trends are explicitly identified, with non-mylonitised and unaltered samples used as references. Sample OUN3 is an ultramylonite, while BDN2 is an altered sample. Samples KNY3, KNY2, and MAN1 are both mylonitised and altered. The various granitoids have an intermediate to felsic composition (SiO_2: 62.21–79.47%). The Al_2O_3 content (11.41–16.62%) is high, while the Na_2O (2.47–4.30%) and K_2O (2.50–7.17%) contents are moderate, with total alkali content ($Na_2O + K_2O$) ranging from 6.80% to 9.74%. The Fe_2O_3 content (5.59–0.88%) and CaO content (3.52–0.49%) are low to moderate, whereas TiO_2 (1.15–0.063%) and MnO (<0.09%) are very low. The MgO contents range from 0.06% to 2.69%, with Mg# of 11.90 to 48.80. Based on normative compositions, the heterogeneous granite plot as syenogranite, monzogranite, and alkali feldspar granite in the Q′–ANOR diagram (Streckeisen and Le Maitre, 1979). The studied granitoids are calc-alkaline, except for GN2 which belongs to the alkaline series (Fig. 12a). The samples follow the Bowen trend in the AFM diagram (see Fig. 10c). According to the geochemical classification of Shand (1943), the granitoids are strongly metaluminous to weakly peraluminous with A/CNK ranging from 0.94 to1.04 (see Figs. 10d). They exhibit high K_2O content and are classified as high-K calc-alkaline to shoshonitic (Fig. 12b). The granitoids range from the ferroan to the magnesian series (Fig. 12c) and plot in the calc-alkali, alkali-calcic and alkalic fields (Fig. 12d). In the Harker diagrams (Fig. 13), the different samples display negative linear to curvilinear correlations between the oxides Al_2O_3, MgO, CaO, TiO_2, P_2O_5 and SiO_2. The SiO_2 vs. Na_2O and SiO_2 vs. K_2O diagrams show dual correlations (Figs. 13c, 13d).

REE and trace elements

Several elements, such as Pb and Cr display a dual trend with differentiation (Figs. 13g, 13h). All granitoids are enriched in LILEs.

Tonalite and granodiorite

The Rb/Sr ratios range from 0.21 to 0.85, and the Rb/Ba ratios from 0.08 to 0.72. HFSE contents are low (Hf: 2.83-6.52 ppm, Ta: 0.40-1.42 ppm, Nb: 7.33-13.0 ppm), except for Zr (104-235 ppm). They are richer in transition metals (Ni: 4.6-17.7 ppm, Cr: 54.2-95.9 ppm, V: 27.1-92.3 ppm) compared to the other granitoids. The ultramylonitized sample has the lowest transition metal content. Primitive mantle-normalized multi-element patterns show negative anomalies in Ba (except for TME1), Nb, Ta, Ce, Sr, P, Zr, and Ti (Fig. 11e); positive anomalies in Rb, Pb, La, Nd. Tonalite sample MOL1 has a positive anomaly in Th. Chondrite-normalized REE patterns (Fig. 11f) show enrichment in LREE [$(La/Yb)_N$ = 6.39-24.01, $(Gd/Yb)_N$ = 1.55-2.22] and negative anomalies in Eu (Eu/Eu* = 0.61-0.62), except for MOL1 (Eu/Eu* = 1.17). The sum of the REEs is 108.15-198.55 ppm.

Heterogeneous granite

The Rb/Sr ratios range from 0.77 to 4.38. The Rb/Ba ratios range from 0.21 to 1.68. The mylonitized and altered syenogranite sample MAN1 and the altered syenogranite sample BDN2 are less rich in LILEs. HFSE contents are low (Hf: 3.08-8.67 ppm, Ta: 0.15-1.43 ppm, Nb: 1.76-9.89 ppm), except for Zr (101-323 ppm).

For monzogranite samples, primitive mantle-normalized multi-element patterns are almost identical, except for NG03b (Fig. 11g). Negative anomalies in Ba, Nb, Ta (except NGN1), Ce, Zr (except NG03b and KNY2), Ti, and positive anomalies in Rb, Th (except NG03b), Pb are observed. Chondrite-normalized REE patterns (Fig. 11h) show negative Eu

550 anomalies, except for NG03b (Eu/Eu* = 2.14). The enrichment in LREE compared with HREE
551 is noticeable, with ratios $(La/Yb)_N$ = 5.38-38.86 and $(Gd/Yb)_N$ = 1.42-3.72. The sum of the
552 REEs is 26.73-155.25 ppm, with the lowest values in NG03b.

553 For the monzogranite and alkali feldspar granite, primitive mantle-normalized multi-
554 element patterns exhibit different shapes (Fig. 11g). The spectra of MAN1, NG03a, and GN2
555 display positive anomalies in Rb, Th, La, Pb, and Nd, and negative anomalies in Ba, Nb, Ta,
556 Sr, Zr (except NG03a), Ti, and Yb. BDN2 (altered biotite syenogranite) shows a sawtooth
557 spectrum due to the recorded alteration. The samples are enriched in LREE compared to HREE
558 [$(La/Yb)_N$ = 20.95-80.65, $(Gd/Yb)_N$ = 1.97-6.3] and have weak negative Eu anomalies (Eu/Eu*
559 = 0.58-0.71). BDN2 exhibits a pseudo-bell curve, positive Eu anomalies (7.08) and is not
560 consistently enriched in LREE compared with HREE (Fig. 11h).

561 **4.4. Whole rock Sr-Nd isotopes**

562 Sr-Nd isotope analyses were performed on two amphibolite samples and two
563 heterogeneous granite samples and the results are presented in Table 3.

564 The two amphibolite samples have distinct $^{87}Rb/^{86}Sr$ ratios of 4.5220837 and
565 0.2113048. The isochron method yields an Rb/Sr age of 610 ± 1 Ma, corresponding to the age
566 of the high temperature Pan-African metamorphism. The $(^{87}Sr/^{86}Sr)_0$ ratio is 0.707611, while
567 the initial $(^{87}Sr/^{86}Sr)_{610}$ ratios are 0.706950 and 0.707580. They have initial $(^{143}Nd/^{144}Nd)_{610}$
568 ratios of 0.511572 and 0.511593. εNd_0 values are -11.33 and -10.71, while εNd_{610} values are -
569 5.46 and -5.05. The T_{DM} ages are 1.702 and 1.701 Ga.

570 The granite have an isochron Rb/Sr age of 781 ± 8 Ma. The $(^{87}Sr/^{86}Sr)_0$ ratio is 0.70528,
571 while the $(^{87}Sr/^{86}Sr)_{655}$ ratios range from 0.709229 to 0.709739. They possess initial
572 $(^{143}Nd/^{144}Nd)_{655}$ ratios of 0.511302 and 0.511379. εNd_0 values are -16.27 and -14.96, and εNd_{654}
573 values are -9.61 and -8.11. The T_{DM} ages are 2.01 and 1.87 Ga.

574 # 5. Discussion

575 ## 5.1. Protoliths of metapyroxenite, amphibolite and paragneiss

576 ### 5.1.1. Nature and source of protoliths of metapyroxenite and amphibolite

577 The calc-alkaline metapyroxenite and amphibolite are characterised by high contents of
578 transition metals (Sc, V, Ni, Co, Cr) and low Th/Sc ratios (0.04–0.05), which imply a ultramafic
579 to mafic igneous protolith. Negative anomalies in Nb, Ti, and Ta, which are high field strength
580 elements (HFSE) relatively immobile in aqueous fluids released from the subducting slab,
581 suggest a suprasubduction mantle source for the magmatic protolith of these rocks. The slight
582 negative anomaly in Ce suggests a contribution from pelagic sediments (Clive and Taylor,
583 1989). This is corroborated by the relatively low to high Rb/Sr ratios (0.07-1.56) and the
584 positive Pb anomaly observed in one sample, which suggest a contribution from the continental
585 crust. The $\varepsilon Nd_{610} < 0$ (–5.46 to –5.05) are comparable to those reported for the Fomopéa
586 amphibolite (εNd_{620} = –3.6 to +1.6; Kwékam et al., 2010) and the Kombé-II amphibolite
587 (Ganwa et al., 2008). The low εNd_{610} combined with enrichment in LREE and LILEs indicates
588 a source from a mantle enriched by elements transferred from aqueous fluids (e.g. Carlson and
589 Irving, 1994; Kwékam et al., 2010). These features suggest that metapyroxenite and
590 amphibolite represent a former juvenile crust formed by partial melting of an enriched mantle,
591 with a significant contribution of crustal material.

592 ### 5.1.2. Protholiths of Paragneiss

593 Paragneiss, deriving from greywackes and metapelites, are characterized by an $S_{0/1}$
594 foliation resulting from the transposition of beds rich in coarse quartz grains alternating with
595 beds rich in ferromagnesian minerals into a schistosity. A protolith made of greywackes and
596 lithic arenites is further supported by their Mg# (34.77 - 38.75), which is close to that of the
597 upper crust (~30; Sammon and McDonough, 2021), as well as by their A/CNK ratios close to

598 1 (1.06-1.08) and low to moderate N/K ratios (2-4.1) (Mendes et al., 2021). The high
599 concentrations of Cr, V, Sc, and Ni indicate a poorly sorted immature protolith containing
600 unstable ferromagnesian minerals. The enrichment in LREE compared to HREE, the negative
601 anomaly in Eu, the ratios La/Sc (1.9-2.6), Th/Sc (0.7-2.2), Th/Co (0.6-2.5), and the positive
602 anomaly in Pb are characteristic of materials originating from remobilization of mafic to felsic
603 materials from the UCC (Cullers, 1995; Taylor and McLennan, 1985). Felsic rocks are enriched
604 in Th while mafic rocks are enriched in Sc (McLennan et al., 1990). In this context, the
605 protoliths of paragneiss are interpreted to represent a detrital sedimentary series derived from
606 erosion of the juvenile crust.

607 **5.2. Genetic links between amphibolite-paragneiss, migmatite, and granitoids from field**
608 **relationships**

609 The diffuse and gradual contacts of amphibolite and paragneiss with migmatite and
610 heterogeneous granite points to a genetic link between these rocks. Partial melting of
611 amphibolite and paragneiss is suggested by their presence as rafts and lenses into the migmatite.
612 The textural continuity of concordant leucosome with veins localized into shear zones, boudins
613 necks and heterogeneous granite (e.g. see Figs. 3b, 3c, 4c, 7a, 7b, 7c, 7e, 7f, 7g, 7h, 7i), is
614 consistent with syn-tectonic melt segregation and migration leading to the formation of an
615 anatectic magma (Burg and Vanderhaeghe, 1993; Brown, 1994; Sawyer, 1999; Vanderhaeghe,
616 2009) during the D_2 deformation phase. Moreover, heterogeneous granite contains layers of
617 mafic minerals (see Figs. 4d) that points to their link with the amphibolite and paragneiss.
618 Overall, these features support the origin of heterogeneous granite through partial melting of
619 amphibolite and paragneiss beyond the metatexite-diatexite transition, under supra-solidus
620 conditions (up to 850 °C) (Brown, 1994; White et al., 2003; Bonzi et al., 2021). The shear zones
621 identified within the migmatite potentially reflect heterogeneous flow of partially molten rocks
622 in response to the combined effects of boundary forces and buoyancy forces related to inverted

density gradients arising from gravitational instabilities (Louis-Napoléon et al., 2024). The wide variability in orientations of the magmatic foliation S_m reflects heterogeneous flow within the partially molten crust in response to gravitational instabilities (McLellan, 1984). The preferential orientation of metamorphic enclaves and the presence of biotite schlierens are evidence of magmatic flow (McCaffrey et al., 1999; Vanderhaeghe, 2001). The magmatic fabrics parallel to the main shear zones together with the deformation continuum from magmatic to solid state are evidence of syn-kinematic emplacement (Vernon, 2004; McCaffrey et al., 1999; Mbounou et al., 2023).

5.3. Petrogenesis of granitoids

5.3.1. Magma evolution processes

The decrease in FeO_t and TiO_2 contents (see Figs. 13b, 13f) is explained by the early crystallization of Fe-oxides and Fe-Ti oxides, which are characteristic of the calc-alkaline series, as further illustrated by the Bowen trend (see Fig. 10c). The tonalite and granodiorite have lower Pb content compared to heterogeneous granite and exhibit different trends in the SiO_2 vs. Pb, SiO_2 vs. Cr, and SiO_2 vs. Co diagrams (Figs. 13g, 13h, 13i), suggesting that they may have originated from a different magma. The dual correlation observed for Na_2O and K_2O oxides with SiO_2 in the syeno-monzogranite is attributed to deformation and hydrothermal processes, primarily occurring in the solid state (not within the scope). Furthermore, samples with more than 72% SiO_2 content have recorded gains in SiO_2 during deformation and alteration processes (Ngassam Mbianya, 2024).

Various studies have shown that the canonical ratios between immobile elements vary little during fractional crystallization but increase significantly during partial melting (e.g., Allègre et al., 1977; Winchester and Floyd, 1977). The La vs. La/Yb, Zr vs. Zr/Nb, and La vs. La/Sm diagrams (Fig. 14) display two evolutionary trends. The tonalite and granodiorite,

together with the diorite and mafic plutonic suite (gabbro, diorite, monzonite) of Deng-Deng (Fossi et al., 2022) and Colomine (Fuh et al., 2021) in eastern Cameroon is interpreted as an evolution through fractional crystallization. A similar trend is identified in amphibolite samples, pointing to a potential genetic link between these rocks through fractional crystallization or partial melting. However, the mafic magmatic rock protolith of the amphibolite has recorded deformation and metamorphism that is not detected in tonalite and granodiorite and thus, they cannot be part of the same magmatic suite. Accordingly, for the Kette district, we favour a model of partial melting of the mafic rocks as the source of the migmatite, heterogeneous granite and tonalite-granodiorite to account for the genetic link between these rocks.

5.3.2. Origin and source of magmas

Heterogeneous granite

The syenogranite, monzogranite and alkali feldspar granite have an Mg# of 11.9-37.3, high Cr content (78.6-185 ppm), low Co content (1.30-3.74 ppm), with 0.39 ppm in altered and mylonitized samples), and low Ni content (2.2-25.1 ppm), which are consistent with a crustal source. They have a lower P_2O_5 content compared to tonalite and granodiorite, similar to that of paragneiss and metatexite migmatite. The rapid decrease in P_2O_5 content with differentiation indicates rocks of infracrustal origin (Chappell and White, 2001). Th/Sc ratios are high (2.6-20.5), with a value below 1 (0.5) only in sample NG03b. The enrichment in LREE, positive anomalies in Pb, Rb, U, and Th, and negative Eu anomalies further support a crustal origin (Clemens and Stevens, 2012), as do the εNd_{654} values of -9.61 and -8.11. In the molar C/FM vs A/FM diagram (Altherr et al., 2000), these rocks are interpreted as products of partial melting of metagreywackes and metapelites, consistent with previous studies in the Eastern Cameroon district (Ngatcha et al., 2019; Azeuda et al., 2022; Lemdjou et al., 2022; Takodjou Wambo et

al., 2024). This interpretation is also in agreement with their position in the SiO_2 vs Mg# diagram (Fig. 15), the petrographic data, and field evidence..

Tonalite and granodiorite

Compared to heterogeneous granitoids, deciphering the origin of tonalite and granodiorite is more challenging. They form small bodies of a few hundred meters in diameter, slightly elongated parallel to the main regional structural trend of the host heterogeneous granitoids, suggesting an intrusion during regional deformation. The Mg# values are relatively high (34.7-48.8), Cr is high (54.2-95.9 ppm), whereas Co (1.04-7.8 ppm) and Ni (4.6-17.7 ppm) are low, close to mantle values. Their chemistry is comparable to that of the Deng-Deng granodiorite and diorites (located a few kilometres from Ketté), which have Mg# values of 38-47 and SiO_2 of 55-68% (Fossi et al., 2022). It is also comparable to the chemistry of the gabbros and diorites from the Colomines basic plutonic suite (BPS), which have Mg# values of 45-58 and SiO_2 of 50-63% (Fuh et al., 2021). The ultramylonitised granodiorite sample OUN3, which deviates from the other granodiorite samples in the Mg# vs. SiO_2 diagram (Fig. 15), is mainly due to an increase in SiO_2 content recorded during mylonitisation (Ngassam Mbianya, 2024). Moreover, the Ketté metapyroxenite and amphibolite display geochemical characteristics similar to those of the basic plutonic suite of Colomines. These different rocks could have originated from the same magma through differentiation processes. The Th/Sc ratios range from 0.5 to 7.5. The high-K signature, negative anomalies in Nb, Ta, and Ti, as well as the LREE and LILE enrichment, are characteristic of a convergent margin environment and an enriched mantle source. The strong positive Pb anomaly is attributed to the assimilation of crustal rocks. Intermediate SiO_2, high Al_2O_3, enriched LREE, moderate HREE, and Na_2O/K_2O ratios > 1 are typical of rocks derived from partial melting of basaltic rocks (Osterhus et al., 2014; Jung et al., 2015).

Collectively, these features together with the regional geological context suggest that these rocks originated either from (1) partial melting of an enriched mantle or (2) melting of the mafic lower crust. Fractional crystallisation of a mafic magma derived from an enriched mantle to produce the granitoids is not favoured by the fact that amphibolite, interpreted as former mafic magmas, are metamorphic rocks and thus have been affected by deformation and metamorphism before the emplacement of the granitoids. Accordingly, partial melting of the amphibolite enclaves is a more likely scenario to produce the tonalite and granodiorite. The εNd(t) values of - 9.0 to - 7.6 and εHf(t) values on zircon ranging from -9.34 to -6.74 obtained on these granodiorite at Doumba Bello (Azeuda et al., 2022; Lemdjou et al., 2022) support a crustal origin. Thus, the tonalite and granodiorite source magmas originated from the melting of amphibolite, whose chemical signature they largely retain. In addition to the field evidence, the presence of intermediate amphibolite containing interstitial quartz and feldspar grains indicates partial melting and/or the percolation of a silicate melt between the amphibole and/or pyroxene phenocrysts. However, the precise mechanisms of their evolution remain to be clarified. These rocks either represent primary melts derived directly from the melting of lower crustal amphibolite or formed through fractional crystallisation of a dioritic liquid produced from such melts. The occurrence of diorite associated with these granodiorite at Ngoura and Colomines (Fuh et al., 2021), together with the chemical data, supports the latter hypothesis. Some metaluminous and magnesian granite could also correspond to more differentiated terms derived from these melts. In conclusion, the diorites, tonalite, and granodiorite of Eastern Cameroon rocks formed dominantly through the fractional crystallisation of a melt derived from the partial melting of mafic lower crust. The source of these rocks is similar to that of the syntectonic magnesian, metaluminous to slightly peraluminous diorites and granodiorite of the Southern Central Zone of the Pan-African Damara Orogen in Namibia (Simon et al., 2017). They are enriched in LREE and have $\varepsilon Nd(t) < 0$, resulting from partial melting of mafic lower

crust that produced dioritic magma, which subsequently evolved through assimilation and fractional crystallisation processes (Jung et al., 2002; Osterhus et al., 2014; Simon et al., 2017; Jung et al., 2020). Experimental studies show that intermediate magmas can be generated by melting hydrous calc-alkaline basaltic rocks in the lower crust (Helz, 1976), with magma composition strongly dependent on whether fluids are present. Partial melting of fluid-absent amphibolite at high temperatures (900–1100 °C) produces dioritic, tonalitic, and granodioritic melts (Beard and Lofgren, 1991; Wolf and Wyllie, 1994; Rapp and Watson, 1995). Dehydration melting of hydrated metabasaltic rocks contributes to the formation of these melts, yielding anhydrous residual assemblages typical of granulitic rocks, rich in plagioclase, orthopyroxene, and clinopyroxene (Beard and Lofgren, 1991). The metapyroxenite observed in outcrops likely correspond to this solid residue. Although magmas generated in the lower crust are generally expected to migrate upwards, the spatial association between restite and intermediate magmas can be explained by several mechanisms. Magma extraction may remain incomplete, with a significant fraction of melt trapped within the restite when the percolation threshold is not significantly exceeded (Vigneresse et al., 1996; Sawyer, 1994, 2001; Brown, 2007). In addition, limited permeability due to the absence of effective migration pathways such as shear zones or fracture networks can significantly hinder melt migration, promoting in situ accumulation and crystallisation (Weinberg, 1999; Paterson and Tobisch, 1992). The relatively high viscosity of intermediate magmas further reduces their segregation and migration, favouring melt retention within the source region (Annen et al., 2006). In some cases, these magmas may represent isolated melt pockets that have not reached the diapiric ascent stage required for large-scale migration (Clemens, 1998; Petford et al., 2000). Finally, during ascent, magmas may entrain fragments of their source rocks, thereby preserving a spatial and textural link between melt and restite (Chappell et al., 1987; White and Chappell, 1997). On the other hand, despite a potential melt fraction beyond the melt percolation threshold, the ubiquitous presence of diatexites in the

744 core crustal scale domes mantled by metatexites attests for the relative inefficiency of melt/solid
745 segregation in the roots of orogenic belts (Burg & Vanderhaeghe, 1993; Withney et al., 2004;
746 Vanderhaeghe, 2009: Kruckenberg et al., 2011; Toé et al., 2013).

747 **6. Conclusion**

748 The data and interpretations presented lead to the following conclusions:

749 (1) The Ketté basement consists of tonalite, granodiorite, granite and alkali feldspar granite
750 including rafts and lenses of amphibolite, metapyroxenite, paragneiss and migmatite.

751 (2) Amphibolite and metapyroxenite are metaluminous (A/CNK: 0.65-0.95) and belong to the
752 calc-alkaline series. They are enriched in LILE, LREE, and have a $\varepsilon Nd_{610} < 0$. They represent
753 a juvenile crust originating from partial melting of an enriched mantle beneath the CAfOB.

754 (3) The paragneiss have parageneses of Hbl+Pl+Kfs+Qtz+Bt. Their protolith is derived from
755 poorly sorted, immature sediments originating from the juvenile crust.

756 (4) The syn-kinematic granitoids are metaluminous to peraluminous (A/CNK: 0.94-1.04), high-
757 K to shoshonitic, and belong to the calc-alkaline and alkaline series. They were emplaced during
758 the syn- to post-collisional stage. The tonalite and granodiorite are interpreted as products of
759 the fractional crystallisation of a melt derived from the dehydration melting of amphibolite with
760 which they are in close contact, with a minor contribution from melts derived from the partial
761 melting of paragneiss. The heterogeneous granite originated from dominant partial melting of
762 metasedimentary rocks composed of paragneiss, consistent with the various metatexitic and
763 diatexitic evolutionary stages observed.

764 (5) The structural record of the Kette district is consistent with progressive deformation under
765 a MP/MT metamorphic gradient reaching partial melting under amphibolite and granulite
766 facies. D_1 and syn-migmatitic phases D_2 are attributed to tectonic accretion contributing to

crustal thickening, with metamorphic peak in the granulite facies (~ 800°C/8-10 kbar), associated with partial melting and migmatite formation; the D_2 phase was also at least partly controlled by gravitational instabilities driving heterogeneous flow of partially molten rocks. The granitoids are emplaced during the progressive phase D_2. The D_3 progressive deformation phase marks the reactivation of the R' MaSZ, leading to the development of a folded mylonitic band.

The Ketté basement represents an exhumed portion of the lower to middle levels of the orogenic root of the Central African Orogenic Belt. The juvenile crust was accreted through the crystallisation of mafic magmas derived from an enriched mantle. It subsequently underwent deformation, metamorphism and thickening due to tectonic accretion, accompanied by partial melting accommodated by shear zones. The segregation, migration and differentiation of melts derived from the partial melting of the mafic lower crust and associated sediments, in varying proportions, led to the formation of different groups of granitoids. These processes contributed to Neoproterozoic crustal growth and crustal reworking-differentiation during the Pan-African orogeny within the Adamawa-Yadé block.

Acknowledgments

The authors express their sincere gratitude to the Mayor of Ketté and to the traditional chiefs of Boubara, Ketté, and Gogoboua for their warm hospitality. We also thank the local guides for their invaluable assistance during fieldwork. Special thanks are extended to Fabienne de Parseval for the preparation of the polished thin sections. We are grateful to the Associate Editor Flavien Choulet, for his valuable comments and suggestions and to the Editor Laurent Jolivet, for overseeing the review process. We also thank the anonymous reviewers for their constructive comments and insightful suggestions, which significantly improved the quality of this manuscript.

Funding

The data presented in this study form part of the PhD thesis of the first author at the University of Dschang, in collaboration with UMR Géosciences Environnement Toulouse (France). The authors gratefully acknowledge the SCAC of the French Embassy in Cameroon and the AUF for financial support provided through the Collège Doctoral Régional MathinBio. This work also forms part of the LithoCOAC project, supported by the CNRS (France) and co-funded through the IRN CNRS FALCoL and the GDRI LithoSud.

Conflicts of interest

The authors declare that they have no competing interests or personal relationships that could have influenced the data presented in this manuscript.

Data availability statement

The data used to support the findings of this study are available from the corresponding author upon request.

Supplementary Material

Table S1. Detection limits for trace elements.

Table S2. Detection limits for major elements.

Figure S1: Geological map with location of figures and sample point.

References

Abdelsalam MG, Liegeois JP, Stern RJ. 2002. The Sahara metacraton. *J Afr Earth Sci* 34:119–136. https://doi.org/10.1016/S0899-5362(02)00013-1

811 Allègre CJ, Treuil M, Minster JF, Minster B, Albarède F. 1977. Systematic use of trace element
812 in igneous process: Part I: Fractional crystallization processes in volcanic suites. *Contrib*
813 *Mineral Petr* 60:57-75. https://doi.org/10.1007/BF00372851

814 Altherr R, Holl A, Hegner E, Langer C, Kreuzer H. 2000. High-potassium, calc-alkaline I-type
815 plutonism in the European Variscides: northern Vosges (France) and northern Schwarzwald
816 (Germany). *Lithos* 50:51–73. https://doi.org/10.1016/S0024-4937(99)00052-3

817 Anders E, Grevesse N. 1989. Abundances of the elements: Meteoritic and solar. *Geochim*
818 *Cosmochim Ac* 53(1):197-214. https://doi.org/10.1016/0016-7037(89)90286-X

819 Annen C, Blundy JD, Sparks RSJ. 2006. The genesis of intermediate and silicic magmas in
820 deep crustal hot zones. *Journal of Petrology* 47:505–539.
821 https://doi.org/10.1093/petrology/egi084

822 Asaah AV, Zoheir B, Lehmann B, Frei D, Burgess R, Suh CE. 2015. Geochemistry and
823 geochronology of the~ 620 Ma gold-associated Batouri granitoids, Cameroon. *Int Geol*
824 *Rev* 57(11-12):1485-1509. https://doi.org/10.1080/00206814.2014.951003

825 Ateh KI, Suh CE, Shemang EM, Vishiti A, Tata E, Chombong NN. 2017. New LA-ICP-MS U-
826 Pb ages, Lu-Hf systematics and REE characterization of zircons from a granitic pluton in the
827 Betare Oya gold district, SE Cameroon. *J Geosci Geomat* 5(6):267-283.
828 https://doi.org/10.12691/jgg-5-6-2

829 Ayonta Kenne P, Ganno S, Ogunyele AC, Wambo JDT, Ngnotué T, Fossi DH, Nzenti JP. 2023.
830 Mantle-crust-interaction and subduction dynamics in Central Cameroon: evidence from the
831 Pan-African Linté microgranular magmatic enclaves (MMEs) and host
832 syenite. *Lithos* 452:107228. https://doi.org/10.1016/j.lithos.2023.107228

833 Azefack Mbounou RL, Ganno S, Ngnotue T, Tanko Njiosseu EL, Fossi DH, Ngassam Mbianya
834 G, Ayonta Kenne P. 2023. Structural and kinematic analysis of the Nkondjock shear zone,
835 central Cameroon: implications on the geodynamic evolution of the Central African Fold
836 Belt. *Arab J Geosci* 16(4):240. https://doi.org/10.1007/s12517-023-11336-x

837 Azeuda Ndonfack KI, Xie Y, Zhong R, Yomeun BS, Cui K, Shan X. 2022. Tectonic evolution
838 of Neoproterozoic rocks, eastern Cameroon: Implication for gold mineralization in the Bétaré
839 Oya and Woumbou–Colomine–Kette districts. *Precambrian Res* 368:106475.
840 https://doi.org/10.1016/j.precamres.2021.106475

841 Beard JS, Lofgren GE. 1991. Dehydration melting and watersaturated melting of basaltic and
842 andesitic greenstones and amphibolites at 1, 3 and 6.9 kbar. *J Petrol* 32:365-402.
843 https://doi.org/10.1093/petrology/32.2.365

844 Blenkinsop TG. 2002. *Deformation Microstructures and Mechanisms in Minerals and Rocks*.
845 New York (USA): Kluwer Academic Publishers, pp. 150. https://doi.org/10.1007/0-306-
846 47543-X

847 Bons PD, Urai JL. 1992. Syn-deformational grain growth: microstructures and kinetics. *J Struct*
848 *Geol* 14:1101–1109. https://doi.org/10.1016/0191-8141(92)90038-X

849 Bonzi WME, Vanderhaeghe O, Van Lichtervelde M, Wenmenga U, André-Mayer AS, Salvi S,
850 Poujol M. 2021. Petrogenetic links between rare metal-bearing pegmatites and TTG gneisses
851 in the West African Craton: The Mangodara district of SW Burkina Faso. *Precambrian*
852 *Res* 364:106359. https://doi.org/10.1016/j.precamres.2021.106359

853 Bouchez JL, Delas C, Gleizes G, Nedélec A, Cuney M. 1992. Submagmatic microfractures in
854 granites. *Geology* 20(1):35-38. https://doi.org/10.1130/0091-
855 7613(1992)020<0035:SMIG>2.3.CO;2

856 Bouyo Houketchang M, Toteu SF, Deloule E, Penaye J, Van Schmus WR. 2009. U-Pb and Sm-
857 Nd dating of high pressure granulite from Tcholliré and Banyo regions, evidence of a Pan-
858 African granulite facies metamorphism in north-central Cameroon. *J Earth Sci* 54:144-154.
859 https://doi.org/10.1016/j.jafrearsci.2009.03.013

860 Bouyo Houketchang M, Zhao Y, Penaye J, Zhang SH, Njel UO. 2015. Neoproterozoic
861 subduction-related metavolcanic and metasedimentary rocks from the Rey Bouba Greenstone
862 Belt of north-central Cameroon in the Central African Fold Belt: new insights into a continental
863 arc geodynamic setting. *Precambrian Res* 261:40-53.
864 https://doi.org/10.1016/j.precamres.2015.01.012

865 Brown M. 1994. The generation, segregation, ascent and emplacement of granite magma: The
866 migmatite-tocrustally-derived granite connection in thickened orogens. *Earth-Sci Rev* 36:83-
867 130. https://doi.org/10.1016/0012-8252(94)90009-4

868 Brown M. 2007. Crustal melting and melt extraction, ascent and emplacement in orogens:
869 mechanisms and consequences. Journal of the Geological Society 164:709–730.
870 https://doi.org/10.1144/0016-76492006-171

871 Burcher K, Grapes R. 2011. *Petrogenesis of metamorphic rocks, eight*. Berlin Heidelberg:
872 Springer-Verlag. https://doi.org/10.1007/978-3-540-74169-5

873 Burg J-P, Vanderhaeghe O. 1993. Structures and way-up criteria in migmatites, with application
874 to the Velay dome (French Massif Central). *J Struct Geol* 15(11):1293-1301.
875 https://doi.org/10.1016/0191-8141(93)90103-H

876 Carignan J, Hild P, Mevelle G, Morel J, Yeghicheyan D. 2001. Routine analyses of trace
877 elements in geological samples using flow injection and low pressure on-line liquid
878 chromatography coupled to ICP-MS: A study of geochemical reference materials BR, DR-N,
879 UB-N, AN-G and GH. *Geostand Newsl* 25(2-3):187-198. https://doi.org/10.1111/j.1751-
880 908X.2001.tb00595.x

881 Carlson RW, Irving AJ. 1994. Depletion and enrichment history of subcontinental lithospheric
882 mantle: an Os, Sr, Nd and Pb isotopic study of ultramafic xenoliths from the northwestern
883 Wyoming Craton. *Earth Planet Sc Lett* 126(4):457-472. https://doi.org/10.1016/0012-
884 821X(94)90124-4

885 Chappell BW, White AJ. 2001. Two contrasting granite types: 25 years later. *Aust J Earth*
886 *Sci* 48(4):489-499. https://doi.org/10.1046/j.1440-0952.2001.00882.x

887 Chappell BW, White AJR, Wyborn D. 1987. The importance of residual source material
888 (restite) in granite petrogenesis. Journal of Petrology 28:1111–1138.
889 https://doi.org/10.1093/petrology/28.6.1111

890 Clemens JD, Stevens G. 2012. What controls chemical variation in granitic
891 magmas?. *Lithos* 134:317-329. https://doi.org/10.1016/j.lithos.2012.01.001

892 Clemens JD. 1998. Observations on the origins and ascent mechanisms of granitic magmas.
893 Journal of the Geological Society 155:843–851. https://doi.org/10.1144/gsjgs.155.5.0843

894 Clive RN, Taylor LA. 1989. A negative Ce anomaly in a peridotite xenolith: Evidence for
895 crustal recycling into the mantle or mantle metasomatism?. *Geochim Cosmochim*
896 *Ac* 53(5):1035-1040. https://doi.org/10.1016/0016-7037(89)90208-1

897 Cox KG, Bell JD, Pankhurst RJ. 1979. *The interpretation of igneous rocks*. London: Georges
898 Allen and Unwin. https://doi.org/10.1007/978-94-017-3373-1

899 Cullers RL. 1995. The controls on the major-and trace-element evolution of shales, siltstones
900 and sandstones of Ordovician to Tertiary age in the Wet Mountains region, Colorado,
901 USA. *Chem Geol* 123(1-4):107-131. https://doi.org/10.1016/0009-2541(95)00050-V

902 Dawaï D, Bouchez JL, Paquette JL, Tchameni R. 2013. The Pan-African quartz-syenite of
903 Guider (north-Cameroon): magnetic fabric and U–Pb dating of a late-orogenic
904 emplacement. *Precambrian Res* 236:132-144. https://doi.org/10.1016/j.precamres.2013.07.008

905 Delor C, Bernard J, Tucker RD, Roig J-Y, Bouyo Houketchang M, Couëffé R, Blein O. 2021.
906 1:1 000 000-scale geological map of Cameroon, second edition. Ministry of Mines, Industry
907 and Technological Development.

908 Djamous GC, Bernard T, Victor M, Ghislain N, Jules T, Gustave BR, Daina JV, Flore MKA,
909 Rosine BC, Charles N. (2026). Petrography and Geochemistry of Syenogranites and
910 Gabbronorites from the Niergui Massif, Guéra Province, Chad. Earth Sciences, 15(2), 109-124.
911 https://doi.org/10.11648/j.earth.20261502.13

912 Djerossem F, Berger J, Vanderhaeghe O, Isseini M, Ganne J, Zeh A. 2020. Neoproterozoic
913 magmatic evolution of the southern Ouaddaï Massif (Chad). *BSGF-Earth Sci Bull* 191(1):34.
914 https://doi.org/10.1051/bsgf/2020032

915 Druguet E. 2019. Deciphering the presence of axial-planar veins in tectonites. *Geosci*
916 *Front* 10(6):2101-2115. https://doi.org/10.1016/j.gsf.2019.02.005

917 Fazio E, Fiannacca P, Russo D, Cirrincione R. 2020. Submagmatic to Solid-State Deformation
918 Microstructures Recorded in Cooling Granitoids during Exhumation of Late-Variscan Crust in
919 North-Eastern Sicily. *Geosciences* 10:311. https://doi.org/10.3390/geosciences10080311

920 Fossi DH, Ganno S, Tankwa NM, Soh Tamehe L, Ayonta Kenné P, Kouayep Tchoundi CL,
921 Kankeu B, Nzenti JP. 2022. Petrogenesis and tectonic setting of the Pan-African Deng-Deng
922 intrusive complex in the Lom series, Eastern Cameroon. *J Afr Earth Sci* 188:104484.
923 https://doi.org/10.1016/j.jafrearsci.2022.104484

924 Frimmel HE. 2008. Earth's continental crustal gold endowment. *Earth Planet Sc Lett* 267:45–
925 55. https://doi.org/10.1016/j.epsl.2007.11.022

926 Frost BR, Barnes CG, Collins WJ, Arculus RJ, Ellis DJ, Frost CD. 2001. A geochemical
927 classification for granitic rocks. *J Petrol* 42(11):2033-2048.
928 https://doi.org/10.1093/petrology/42.11.2033

929 Fuh CG, Tchakounte NJ, Kundu OM, Tchop JL, Nkoumbou C. 2021. Four Pan-African
930 plutonic sets of the Colomines gold district (East-Cameroon): Petrogenesis, K-Ar dating and
931 geodynamic significance. *J Afr Earth Sci* 181:104220.
932 https://doi.org/10.1016/j.jafrearsci.2021.104220

933 Ganwa AA, Frisch W, Siebel W, Shang CK, Mvondo Ondoa J, Satir M, Tchakounté Numbem
934 J. 2008. Zircon 207Pb/206Pb evaporation ages of Panafrican metasedimentary rocks in the
935 Kombé-II area (Bafia Group, Cameroon): constraints on protolith age and provenance. *J Afr*
936 *Earth Sci* 51:77–88. https://doi.org/10.1016/j.jafrearsci.2007.12.003

937 Ganwa AA, Klötzli US, Hauzenberger C. 2016. Evidence for Archean inheritance in the pre-
938 Panafrican crust of Central Cameroon: Insight from zircon internal structure and LA-MC-ICP-
939 MS UPb ages. *J Afr Earth Sci* 120:12–22. https://doi.org/10.1016/j.jafrearsci.2016.04.013

940 Geringer GJ. 1979. The origin and tectonic setting of amphibolites in part of the Namaqua
941 metamorphic belt, South Africa. *S Afr J Geol* 82(3):287-303.

942 Goldfarb RJ, Groves DI, Gardoll S. 2001. Orogenic gold and geologic time: a global
943 synthesis. *Ore Geol Rev* 18:1–75. https://doi.org/10.1016/S0169-1368(01)00016-6

944 Hamdja Ngoniri A, Dadjo Djomo H, Ngnotue T, Ayonta Kenne P, Mbianya G, Ganno S, Nzenti
945 JP. 2021. Zircon Trace Element Geochemistry and Ti-in-Zircon Thermometry of the Ngazi-
946 Tina Pan-African Post-Collisional Granitoids, Adamawa Cameroon. *Int J Geosci* 12:307–328.
947 DOI: 10.4236/ijg.2021.124017

948 Helz R. 1976. Phase relations of basalt in their melting ranges at P H2O=5 kb: Part 2. Melt
949 compositions. *J Petrol* 17:139-193. https://doi.org/10.1093/petrology/17.2.139

950 Herron MM. 1988. Geochemical classification of terrigenous sands and shales from core or log
951 data. *J Sediment Res* 58(5):820-829. https://doi.org/10.1306/212F8E77-2B24-11D7-
952 8648000102C1865D

953 Irvine TN, Baragar WRA. 1971. A guide to the chemical classification of the common volcanic
954 rocks. *Can J Earth Sci* 8:523-548. https://doi.org/10.1139/e71-055

955 Isseini M, André-Mayer AS, Vanderhaeghe O, Barbey P, Deloule E. 2012. A-type granites
956 from the Pan-African orogenic belt in south-western Chad constrained using geochemistry, Sr–
957 Nd isotopes and U–Pb geochronology. *Lithos* 153:39-52.
958 https://doi.org/10.1016/j.lithos.2012.07.014

959 Jacob JB, Moyen JF, Fiannacca P, Laurent O, Bachmann O, Janoušek V, Villaros A. 2021.
960 Crustal melting vs. fractionation of basaltic magmas: Part 2, Attempting to quantify mantle and
961 crustal contributions in granitoids. *Lithos* 402:106292.
962 https://doi.org/10.1016/j.lithos.2021.106292

963 Jung S, Hoernes S, Mezger K. 2002. Synorogenic melting of mafic lower crust; constraints
964 from geochronology, petrology and Sr, Nd, Pb and O isotope geochemistry of quartz diorites
965 (Damara Orogen, Namibia). *Contrib Mineral Petr* 143:551-566.
966 https://doi.org/10.1007/s00410-002-0366-5

967 Jung S, Kröner A, Hauff F, Masberg P. 2015. Sr–Nd–Pb isotope composition of syn-orogenic
968 diorite–granodiorite–granite complexes: mantle lithosphere–crust interaction vs. melting of
969 mafic lower crust. *J Afr Earth Sci* 101:253-265. https://doi.org/10.1016/j.jafrearsci.2014.09.015

970 Jung S, Romer RL, Pfänder JA, Berndt J. 2020. Petrogenesis of early syn-tectonic monzonite-
971 granodiorite complexes–Crustal reprocessing versus crustal growth. *Precambrian*
972 *Res* 351:105957. https://doi.org/10.1016/j.precamres.2020.105957

973 Kamguia Kamani MS, Wang W, Tchouankoue JP, Huang S-F, Yomeun B, Xue EK, Lu GM.
974 2021. Neoproterozoic syn-collision magmatism in the Nkondjock region at the northern border
975 of the Congo craton in Cameroon: Geodynamic implications for the Central African orogenic
976 belt. *Precambrian Res* 353:106015. https://doi.org/10.1016/j.precamres.2020.106015

977 Kankeu B, Greiling RO, Nzenti JP. 2009. Pan-African strike-slip tectonics in eastern Cameroon
978 - magnetic fabrics (AMS) and structure in the Lom basin and its gneissic
979 basement. *Precambrian Res* 174(3):258-272. https://doi.org/10.1016/j.precamres.2009.08.001

980 Kankeu B, Greiling RO. 2006. Magnetic fabrics (AMS) and transpression in the Neoproterozoic
981 basement of Eastern Cameroon (Garga-Sarali area). *Neues Jahrb Geol P M* 239(2):263–287.
982 DOI: 10.1127/njgpa/239/2006/263

983 Kouo AFM, Tassongwa B, Metang V, Mbianya GN, Tchanamou DMF, Mbouagouoré LM,
984 Fotso DK, Wouatong ASL. (2026). A Multisource Remote Sensing–Fuzzy Logic Framework
985 for Uranium Exploration in the Newly Identified Bangoua Prospect, Cameroon. *Sci Afr* e03202.
986 https://doi.org/10.1016/j.sciaf.2026.e03202

987 Kouske AP, Gerard M, Etame J, Kanouo NG, Tchouatcha MS, Ghogomu TR, Cuney M, Cheo
988 SE, Ngako V. 2022. Paragenesis, mineral chemical and microtextural studies of uranium
989 bearing minerals in the brecciated albitites U-ores from the Kitongo shear zone, Poli region,
990 northern Cameroon. *Int J Earth Sci* 111:1413-1436. https://doi.org/10.1007/s00531-022-
991 02186-1

992 Kröner A, Stern RJ. 2004. Pan-African Orogeny. In: *Encyclopedia of Geology*. Volume 1.
993 Elsevier, pp. 1-12. https://doi.org/10.1016/B0-12-369396-9/00431-7

994 Kruckenberg SC, Vanderhaeghe O, Ferré EC, Teyssier C, Whitney DL. 2011. Flow of partially
995 molten crust and the internal dynamics of a migmatite dome, Naxos, Greece. *Tectonics*
996 30:TC3001. https://doi.org/10.1029/2010TC002751

997 Kwékam M, Liégeois JP, Njonfang E, Affaton P, Hartmann G, Tchoua F. 2010. Nature, origin
998 and significance of the Fomopéa Pan-African high-K calc-alkaline plutonic complex in the
999 Central African fold belt (Cameroon). *J Afr Earth Sci* 57:79-95.
1000 https://doi.org/10.1016/j.jafrearsci.2009.07.012

1001 Lemdjou YB, Li H, Whattam SA, Azeuda Ndonfack KI, Tchato Tchaptchet DPI, Ketchaya YB,
1002 Dongmo Nguimatsia FW. 2022. Petrogenesis, tectonic setting and geodynamic implications of
1003 Ouaden, Doumba Bello, and Ngoura granitic plutons (Eastern Cameroon): Constraints from
1004 elemental and Sr−Nd−Hf isotopic data and zircon U−Pb ages. *Lithos* 418:106682.
1005 https://doi.org/10.1016/j.lithos.2022.106682

1006 Liégeois J-P, Abdelsalam MG, Ennih N, Ouabadi A. 2013. Metacraton: Nature, genesis and
1007 behavior. *Gondwana Res* 23:220-237. https://doi.org/10.1016/j.gr.2012.02.016

1008 Louis-Napoléon A, Vanderhaeghe O, Gerbault M, Martin R, Bonometti T. 2024. Formation of
1009 the Naxos nested domes and crustal differentiation by convection and diapirism. *BSGF-Earth*
1010 *Sci Bull* 195(1):21. https://doi.org/10.1051/bsgf/2024017

1011 Luais B, Telouk P, Albaréde F. 1997. Precise and accurate neodymium isotopic measurements
1012 by plasma-source mass spectrometry. *Geochim Cosmochim Ac* 61(22):4847-4854.
1013 https://doi.org/10.1016/S0016-7037(97)00293-7

1014 Mbounou RLA, Tchuifong ABK, Ganno S, Ngassam-Mbianya G, Nono GDK, Njiosseu ELT,
1015 Ngnotue T. 2026. Shear zone evolution and regional strain implications during emplacement of
1016 the Nkondjock plutonic massif, Nyong-Bayomen Domain, Central African Orogenic Belt. *J Afr*
1017 *Earth Sci* 106144. https://doi.org/10.1016/j.jafrearsci.2026.106144

1018 McCaffrey KJW, Miller CF, Karlstrom KE, Simpson C. 1999. Synmagmatic deformation
1019 patterns in the Old Woman Mountains, SE California. *J Struct Geol* 21:335–349.
1020 https://doi.org/10.1016/S0191-8141 (98)00107-2

1021 McDonough WF, Sun SS. 1995. The composition of the Earth. *Chem Geol* 120(3-4):223-253.
1022 https://doi.org/10.1016/0009-2541(94)00140-4

McLellan E. 1984. Deformational behaviour of migmatites and problems of structural analysis in migmatite terrains. *Geol Mag* 121(4):339-345. https://doi.org/10.1017/S001675680002923X

McLennan SM, Taylor SR, McCulloch MT, Maynard JB. 1990. Geochemical and Nd-Sr isotopic composition of deep-sea turbidites: crustal evolution and plate tectonic associations. *Geochim Cosmochim Ac* 54(7):2015-2050. https://doi.org/10.1016/0016-7037(90)90269-Q

Mendes LDC, dos Santos TJS, Gomes NB. 2021. Geochemistry and provenance of the metasedimentary rocks surrounding the Santa Quitéria magmatic arc, NE Brazil: Tectonic and paleogeographic implications for the assembly of West Gondwana. *Precambrian Res* 356:106063. https://doi.org/10.1016/j.precamres.2020.106063

Motto Mbita AS, Tankwa MN, Tamehe LS, Fossi DH, Tchoupe GBT, Ganno S, Nzenti JP. 2024. Source and age of the Ngaye banded iron formations, Adamawa Yadé Domain, Central Cameroon: Constraints from whole-rock geochemistry and U-Pb zircon geochronology. *Geochemistry* 84(3):126173. https://doi.org/10.1016/j.chemer.2024.126173

Moyen JF, Janoušek V, Laurent O, Bachmann O, Jacob JB, Farina F, Villaros A. 2021. Crustal melting vs. fractionation of basaltic magmas: Part 1, granites and paradigms. *Lithos* 402:106291. https://doi.org/10.1016/j.lithos.2021.106291

Nesbitt HW, Young GM. 1989. Formation and diagenesis of weathering profiles. *J Geol* 97(2):129-147. https://www.jstor.org/stable/30065535

Ngako V, Affaton P, Njonfang E. 2008. Pan-African tectonics in northwestern Cameroon: implication for the history of western Gondwana. *Gondwana Res* 14(3):509-522. https://doi.org/10.1016/j.gr.2008.02.002

1045 Ngako V, Affaton P, Nnange JM, Njanko T. 2003. Pan-African tectonic evolution in central
1046 and southern Cameroon: transpression and transtension during sinistral shear movements. *J Afr*
1047 *Earth Sci* 36(3):207-214. https://doi.org/10.1016/S0899-5362(03)00023-X

1048 Ngassam Mbianya G, Ngnotue T, Takodjou Wambo JD, Ganno S, Pour AB, Ayonta Kenne P,
1049 Fossi DH, Wolf ID. 2021. Remote sensing satellite-based structural/alteration mapping for gold
1050 exploration in the Ketté goldfield, Eastern Cameroon. *J Afr Earth Sci* 184:104386.
1051 https://doi.org/10.1016/j.jafrearsci.2021.104386

1052 Ngassam Mbianya G. 2024. Etude des formations Précambriennes de Ketté (Est-Cameroun) et
1053 implications métallogéniques. PhD Thesis *University of Dschang (Cameroon)*

1054 Ngatcha RB, Okunlola OA, Suh CE, Ateh KI, Hofmann A. 2019. Petrochemical
1055 characterization of Neoproterozoic Colomine granitoids, SE Cameroon: implications for gold
1056 mineralization. *Lithos* 344–345:175–192. https://doi.org/10.1016/j.lithos.2019.06.028

1057 Ngnotué T, Nzenti JP, Barbey P, Tchoua FM. 2000. The Ntui-Betamba highgrade gneisses: a
1058 Northward extension of the Pan-African Yaounde gneisses in Cameroon. *J Afr Earth*
1059 *Sci* 31:369–381. https://doi.org/10.1016/S0899-5362(00)00094-4

1060 Ngounouno FY, Nomo Negue E, Kolb J, Walter B, Teda Soh AC, Patten C, Ngounouno I. 2022.
1061 Tectonic setting, fluid inclusion and gold mineralization of the southwest Poli region (northern
1062 Cameroon Domain). *J Afr Earth Sci* 194:104579.
1063 https://doi.org/10.1016/j.jafrearsci.2022.104579

1064 Nkoumbou C, Barbey P, Yonta-Ngouné C, Paquette JL, Villiéras F. 2014. Pre-collisional
1065 geodynamic context of the southern margin of the Pan-African fold belt in Cameroon. *J Afr*
1066 *Earth Sci* 99:245-260. https://doi.org/10.1016/j.jafrearsci.2013.10.002

1067 Nomo Negue E, Takodjou Wambo JD, Yamgouot Ngounouno F, Negou Nembouet J, Teda Soh
1068 AC, Tsassé Nganno AS, Fossi DH, Tchameni R. 2021. Searching gold origin through litho-
1069 structural analysis and morphological characterization of alluvial gold nuggets in the Guiwa-
1070 Yangamo area (Batouri goldfield, Eastern Cameroon). *Arab J Geosci* 14:1973.
1071 https://doi.org/10.1007/s12517-021-07799-5

1072 Nomo Negué E, Tchameni R, Vanderhaeghe O, Sun F, Barbey P, Tekoum L, Fouotsa NAS.
1073 2017. Structure and LA-ICP-MS zircon U–Pb dating of syntectonic plutons emplaced in the
1074 Pan-African Banyo-Tcholliré shear zone (central north Cameroon). *J Afr Earth Sci* 131:251-
1075 271. https://doi.org/10.1016/j.jafrearsci.2017.04.002

1076 Nzenti JP, Barbey P, Macaudiere J, Soba D. 1988. Origin and evolution of the late precambrian
1077 high-grade Yaounde Gneisses (Cameroon). *Precambrian Res* 38:91–109.
1078 https://doi.org/10.1016/0301-9268(88)90086-1

1079 Nzenti JP, Kapajika B, Wörner G, Lubala TR. 2006. Synkinematic emplacement of granitoids
1080 in a Pan-African shear zone in Central Cameroon. *J Afr Earth Sci* 45:74–86.
1081 https://doi.org/10.1016/j.jafrearsci.2006.01.005

1082 Osterhus L, Jung S, Berndt J, Hauff F. 2014. Geochronology, geochemistry and Nd, Sr and Pb
1083 isotopes of syn-orogenic granodiorites and granites (Damara orogen, Namibia) - arc-related
1084 plutonism or melting of mafic crustal sources?. *Lithos* 200-201:386-401.
1085 https://doi.org/10.1016/j.lithos.2014.05.002

1086 Owona S, Ondoa JM, Ratschbacher L, Ndzana SPM, Tchoua FM, Ekodeck GE. 2011. The
1087 geometry of the Archean, Paleo-and Neoproterozoic tectonics in the Southwest Cameroon. *CR*
1088 *Geosci* 343(4):312-322. https://doi.org/10.1016/j.crte.2010.12.008

1089 Passchier CW, Trouw RAJ. 2005. *Microtectonics*. 2nd edition. Springer, p. 371.
1090 https://doi.org/10.1007/3-540-29359-0

1091 Paterson SR, Tobisch OT. 1992. Rates of processes in magmatic arcs: implications for the
1092 timing and nature of pluton emplacement and wall-rock deformation. Journal of Structural
1093 Geology 14:291–300. https://doi.org/10.1016/0191-8141(92)90087-D

1094 Peccerillo A, Taylor SR. 1976. Geochemistry of eocene calc-alkaline volcanic rocks from the
1095 Kastamonu area, Northern Turkey. *Contrib Mineral Petr* 58:63–81.
1096 https://doi.org/10.1007/BF00384745

1097 Penaye J, Kröner A, Toteu SF, Van Schmus WR, Doumnang J-C. 2006. Evolution of the Mayo
1098 Kebbi region as revealed by zircon dating: An early (ca. 740Ma) Pan-African magmatic arc in
1099 southwestern Chad. *J Afr Earth Sci* 44:530–542.
1100 https://doi.org/10.1016/j.jafrearsci.2005.11.018

1101 Penaye J, Toteu SF, Van Schmus WR, Nzenti JP. 1993. U-Pb and Sm-Nd preliminary
1102 geochronologic data on the Yaoundé series, Cameroon: reinterpretation of the granulitic rocks
1103 as the suture of a collision in the "Centrafrican belt". *CR Acad Sci Paris* 317:789–794.

1104 Petford N, Cruden AR, McCaffrey KJW, Vigneresse JL. 2000. Granite magma formation,
1105 transport and emplacement in the Earth's crust. Nature 408:669–673.
1106 https://doi.org/10.1038/35047000

1107 Rapp RP, Watson EB. 1995. Dehydration melting of metabasalt at 8 – 32 kbar: implications for
1108 continental growth and crust – mantle recycling. *J Petrol* 36:891–932.
1109 https://doi.org/10.1093/petrology/36.4.891

1110 Roser BP, Korsch RJ. 1988. Provenance signatures of sandstone-mudstone suites determined
1111 using discriminant function analysis of major-element data. *Chem Geol* 67(1-2):119-139.
1112 https://doi.org/10.1016/0009-2541(88)90010-1

1113 Saha-Fouotsa AN, Vanderhaeghe O, Barbey P, Eglinger A, Tchameni R, Zeh A, Nomo EN.
1114 2019. The geologic record of the exhumed root of the Central African Orogenic Belt in the
1115 central Cameroon domain (Mbé–Sassa-Mbersi region). *J Afr Earth Sci* 151:286-314.
1116 https://doi.org/10.1016/j.jafrearsci.2018.12.008

1117 Sammon LG, McDonough WF. 2021. A geochemical review of amphibolite, granulite, and
1118 eclogite facies lithologies: Perspectives on the deep continental crust. *J Geophys Res-Sol*
1119 *Ea* 126(12):e2021JB022791. https://doi.org/10.1029/2021JB022791

1120 Sawyer EW. 1994. Melt segregation in the continental crust. Geology 22:1019–1022.
1121 https://doi.org/10.1130/0091-7613(1994)022<1019:MSITCC>2.3.CO;2

1122 Sawyer EW. 1999. Criteria for the recognition of partial melting. *Phys Chem Earth Pt*
1123 *A* 24(3):269-279. https://doi.org/10.1016/S1464-1895(99)00029-0

1124 Shand SJ. 1943. *Eruptive rocks. Their genesis, composition, classification, and their relations*
1125 *to ore-deposits*. New York: Wiley, 444 pp.

1126 Shellnutt JG, Pham NHT, Denyszyn SW, Yeh MW, Lee TY. 2017. Timing of collisional and
1127 post-collisional Pan-African Orogeny silicic magmatism in south-central Chad. *Precambrian*
1128 *Res* 301:113-123. https://doi.org/10.1016/j.precamres.2017.08.021

1129 Simon I, Jung S, Romer RL, Garbe-Schönberg D, Berndt J. 2017. Geochemical and Nd-Sr-Pb
1130 isotope characteristics of synorogenic lower crust-derived granitoids (Central Damara orogen,
1131 Namibia). *Lithos* 274-275:397-411. https://doi.org/10.1016/j.lithos.2016.12.033

1132 Soba D. 1991. U-Pb, SmNd and Rb-Sr dating in the Pan-African Mobile Belt of Eastern
1133 Cameroon: Upper Proterozoic age of the Lom series. *CR Acad Sci Paris* 312:1453-1458.

1134 Stipp M, Stünitz H, Heilbronner R, Schmid SM. 2002a. Dynamic recrystallization of quartz:
1135 correlation between natural and experimental conditions. *Geological Society, London, Special*
1136 *Publication* 200: 171–190. https://doi.org/10.1144/GSL.SP.2001.200.01.11

1137 Stipp M, Stünitz H, Heilbronner R, Schmid SM. 2002b. The eastern Tonale fault zone: a
1138 "natural laboratory" for crystal plastic deformation of quartz over a temperature range from 250
1139 to 700◦C. *J Struct Geol* 24:1861–1884. https://doi.org/10.1016/S0191-8141(02)00035-4

1140 Streckeisen A, Le Maitre RW. 1979. A chemical approximation to the modal QAPF
1141 classification of the igneous rocks. *Neues Jahrb Geol P M* 134:169-190.

1142 Suh CE, Lehmann B, Mafany GT. 2006. Geology and geochemical aspects of lode gold
1143 mineralization at Dimako-Mboscorro, SE Cameroon. *Geochem-Explor Env A* 6:295–309.
1144 http://dx.doi.org/10.1144/1467-7873/06-110

1145 Takodjou Wambo JD, Roy A, Ganno S, Fossi DH, Wilner OD, Nzenti JP, Asimow PD. 2024.
1146 Single-zircon UPb geochronology and petrogenesis of Pan-African granitoids associated with
1147 gold-bearing quartz veins in the Ngoura-Colomines area, Eastern
1148 Cameroon. *Lithos* 472:107553. https://doi.org/10.1016/j.lithos.2024.107553

1149 Tanko Njiosseu EL, Nzenti JP, Njanko T, Kapajika B, Nedelec A. 2005. New UPb Zircon ages
1150 from Tonga (Cameroon): coexisting Eburnean Transamazonian (2.1 Ga) and pan-African (0, 6
1151 Ga) imprints. *CR Geosci* 337:551–562. https://doi.org/10.1016/j.crte.2005.02.005

1152 Tata E, Suh CE, Vishiti A, Shemang EM, Fon NA, Ateh KI, Chombo NN. 2018. Wallrock
1153 alteration categories and their geochemical signatures in gold-bearing Neoproterozoic

granitoids, Batouri gold district, southeastern Cameroon. *Geochem-Explor Env A* 19:269-288. https://doi.org/10.1144/geea2016-017

Taylor SR, McLennan SM. 1985. *The continental crust: its composition and evolution*. Oxford: Blackwell Scientific.

Tchakounté J, Eglinger A, Toteu SF, Zeh A, Nkoumbou C, Mvondo-Ondoa J, Penaye J, de Wit M, Barbey P. 2017. The Adamawa-Yadé domain, a piece of Archaean crust in the Neoproterozoic Central African Orogenic belt (Bafia area, Cameroon). *Precambrian Res* 299:210–229. https://doi.org/10.1016/j.precamres.2017.07.001

Tcheumenak Kouémo J, Fozing EM, Zagalo Al-hadj H, Noudiedie Kamgang JA, Kwékam M, Njonfang E. 2023. Structural and petrographic characterization of the Fotouni-Kekem Shear Zone: implication for P–T-t regional metamorphism and mylonitic evolutions along the Central Cameroon Shear Zone. *Arab J Geosci* 16:38. https://doi.org/10.1007/s12517-022-11095-1

Tchouankoue JP, Li XH, Belnoun RNN, Mouafo L, Ferreira VP. 2016. Timing and tectonic implications of the Pan-African Bangangte syenomonzonite, West Cameroon: Constraints from in-situ zircon U-Pb age and Hf-O isotopes. *J Afr Earth Sci* 124:94-103. https://doi.org/10.1016/j.jafrearsci.2016.09.009

Tchoupe GBT, Ndime EN, Fossi DH, Djoukouo AS, Tchouatcha MS, Motto SAM, Nzenti JP. 2024. Mineralization of Zr-REE-Y in the Ngaoumbol iron formations, central Cameroon: Insights from petrography, mineral chemistry and whole rock geochemistry. *Solid Earth Sci* 9(2):100178. https://doi.org/10.1016/j.sesci.2024.100178

1174 Toé W, Vanderhaeghe O, André-Mayer AS, Feybesse JL, Milési JP. 2013. From migmatites to
1175 granites in the Pan-African Damara orogenic belt, Namibia. *J Afr Earth Sci* 85:62-74.
1176 http://dx.doi.org/10.1016/j.jafrearsci.2013.04.009

1177 Topien RM, Moloto-A-Kenguemba G, Traore M, Rajendran S, Kouassi BR. 2023. Litho-
1178 structural mapping and structural evolution of the Bocaranga pluton, northwest Adamawa-Yadé
1179 domain, Central African Republic. *J Afr Earth Sci* 198:104793.
1180 https://doi.org/10.1016/j.jafrearsci.2022.104793

1181 Toteu SF, Penaye J, Deloule E, Van Schmus WR, Tchameni R. 2006. Diachronous evolution
1182 of volcano-sedimentary basins north of the Congo craton: Insights from U–Pb ion microprobe
1183 dating of zircons from the Poli, Lom and Yaoundé Groups (Cameroon). *J Afr Earth Sci* 44:428–
1184 442. https://doi.org/10.1016/j.jafrearsci.2005.11.011.

1185 Toteu SF, Penaye J, Poudjom Djomani Y. 2004. Geodynamic evolution of the Pan-African belt
1186 in central Africa with special reference to Cameroon. *Can J Earth Sci* 41(1):73-85.
1187 https://doi.org/10.1139/e03-079

1188 Toteu SF, Wit M, Penaye J, Drost K, Tait JA, Houketchang Bouyo M, Van Schmus WR, Jelsma
1189 H, Moloto-A-Kenguemba GR, Francisco da Silva Filho A, Lerouge C, Doucouré M. 2022.
1190 Geochronology and correlations in the Central African Fold Belt along the northern edge of the
1191 Congo Craton: new insights from U-Pb dating of zircons from Cameroon, Central African
1192 Republic, and south-western Chad. *Gondwana Res* 107:296-324.
1193 https://doi.org/10.1016/j.gr.2022.03.010

1194 Van Schmus WR, Oliveira EP, da Silva Filho AF, Toteu SF, Penaye J, Guimaraes IP. 2008.
1195 Proterozoic links between the Borborema Province, NE Brazil, and the Central African Fold
1196 Belt. In: Pankhurst RJ, Trouw RAJ, Brito Neves BB, De Wit MJ (Eds). *West Gondwana: Pre-*

1197 *Cenozoic Correlations Across the South Atlantic Region*. Volume 294. Geological Society,
1198 London, Special Publications, pp. 69–99. https://doi.org/10.1144/sp294.5.

1199 Vanderhaeghe O, Teyssier C. 1997. Formation of the Shuswap metamorphic core complex
1200 during late-orogenic collapse of the Canadian Cordillera: role of ductile thinning and partial
1201 melting of the mid- to lower crust. *Geodin Acta* 10(2):41–58.
1202 https://doi.org/10.1080/09853111.1997.11105292

1203 Vanderhaeghe O. 2001. Melt segregation, pervasive melt migration and magma mobility in the
1204 continental crust: the structural record from pores to orogens. *Phys Chem Earth Pt A* 26:213-
1205 223. https://doi.org/10.1016/S1464-1895(01)00048-5

1206 Vanderhaeghe O. 2009. Migmatites, granites and orogeny: flow modes of partially molten rocks
1207 and magmas associated with melt/solid segregation in orogenic belts. *Tectonophysics* 477:119–
1208 134. https://doi.org/10.1016/j.tecto.2009.06.021

1209 Vernon RH. 2004. *A practical guide to rock microstructure*. Cambridge: Cambridge University
1210 Press, 578 pp. https://doi.org/10.1017/CBO9780511807206

1211 Vigneresse JL, Barbey P, Cuney M. 1996. Rheological transitions during partial melting and
1212 crystallization with application to felsic magma segregation and transfer. Journal of Petrology
1213 37:1579–1600. https://doi.org/10.1093/petrology/37.6.1579

1214 Vishiti A, Suh CE, Lehmann B, Shemang EM, Ngome NLJ, Nshanji NJ, Chinjo EF, Mongwe
1215 OY, Egbe AJ, Petersen S. 2018. Mineral chemistry, bulk rock geochemistry, and S-isotope
1216 signature of lode-gold mineralization in the Bétaré-Oya gold district, south-east
1217 Cameroon. *Geol J* 53(6):2579–2596. https://doi.org/10.1002/gj.3093

1218 Weinberg RF. 1999. Mesoscale pervasive felsic magma migration: alternatives to dyking.
1219 Lithos 46:393–410. https://doi.org/10.1016/S0024-4937(98)00075-9

1220 White AJR, Chappell BW. 1977. Ultrametamorphism and granitoid genesis. Tectonophysics
1221 43:7–22. 10.1016/0040-1951(77)90003-8

1222 White RW, Powell R, Clarke GL. 2003. Prograde metamorphic assemblage evolution during
1223 partial melting of metasedimentary rocks at low pressures: migmatites from Mt Stafford,
1224 Central Australia. *J Petrol* 44(11):1937-1960. https://doi.org/10.1093/petrology/egg065

1225 Whitney DL, Teyssier C, Vanderhaeghe O. 2004. Gneiss domes and crustal flow. In: Whitney
1226 DL, Teyssier C, Siddoway CS, eds. Gneiss domes in orogeny. *Geological Society of America*
1227 *Special Paper* 380:15–33. https://doi.org/10.1130/0-8137-2380-9.15

1228 Winchester JA, Floyd PA. 1977. Geochemical discrimination of different magma series and
1229 their differentiation products using immobile elements. *Chem Geol* 20:325-343.
1230 https://doi.org/10.1016/0009-2541(77)90057-2

1231 Wolf MB, Wyllie PJ. 1994. Dehydration-melting of amphibolite at 10 kbar: the effects of
1232 temperature and time. *Contrib Mineral Petr* 115:369–383.
1233 https://doi.org/10.1007/BF00320972

1234 **Figure captions**

1235 **Figure 1.** Geological map: a) Cameroon (modified from Toteu et al., 2022 and Kouo et al.,
1236 2026); b) Eastern Cameroon (modified from Delor et al., 2021); Age data are from: Soba et al.
1237 (1991), Toteu et al. (2006), Asaah et al. (2015), Ateh et al. (2017), Fuh et al. (2021), Azeuda et
1238 al. (2022), Lemdjou et al. (2022). TBSZ: Tcholliré-Banyo Shear Zone, CCSZ: Central

1239 Cameroon Shear Zone, SF: Sanaga Fault, NBSZ; Ngoro Bélabo Shear Zone, MGSZ:
1240 Messaména-Gribi Shear Zone.

1241 **Figure 2.** Geological map (modified from Ngassam Mbianya et al., 2021).

1242 **Figure 3.** Photographs and microphotographs of metamorphic rocks: a) metapyroxenite enclave
1243 in granodiorite; b) metatexitic amphibolite; c) amphibolite and paragneiss enclaves in diffuse
1244 contact with heterogeneous biotite granite interpreted as a diatexite. Cross polarized view of (d)
1245 metapyroxenite with heterogranular granoblastic microstructure; (e) amphibolite with
1246 hornblende-plagioclase-biotite and interstitial quartz; (f) amphibole and pyroxene paragneiss
1247 with granoblastic heterogranular microstructure; and (g) biotite and amphibole paragneiss
1248 grano-lepidoblastic microstructure.

1249 **Figure 4.** Photographs and microphotographs of migmatite: a) migmatitic foliation S_{mgm} in a
1250 metatexite; b) microstructure of alternating leucosome and mesosome layers in a metatexite;
1251 c) migmatite (metatexite - diatexite transition) with interconnected leucosome networks; d)
1252 Diatexite consisting of biotite and amphibole heterogeneous granite.

1253 **Figure 5.** Photographs and microphotographs of granitoids: a) magmatic foliation in tonalite;
1254 b) S_m/C magmatic fabric; c) σ mantle porphyroclats into protolymonitic heterogeneous granite;
1255 d) myrmekite and perthite in tonalite; e) spo highlighting the S_m foliation; f) granite with a
1256 magmatic fabric marked by imbricated deformed phenocrysts; g) melt-filled fracture.

1257 **Figure 6.** Microstructures of Mama Shear Zone: a) S_{myl}/C_{n+2} fabric of a mylonite; b)
1258 ultramylonitic foliation S_{myl}; c) S_{myl}/C_{n+2} fabric of a mylonite, marked by the preferred
1259 orientation of quartz ribbons with serrated grain boundaries and an undulose extinction, and by
1260 biotite porphyroclasts with a sigma shape consistent with a sinistral sense of shear; d) amoeboid
1261 quartz grains; e) asymmetric grain with lobate borders; f) asymmetric alkali feldspar grains with

bulges; g) quartz grains with grain boundaries at 120 °; h) porphyroclasts and multi-grain composite clasts embedded in finely recrystallized matrix, and alternating beds in an ultramylonite granodiorite.

Figure 7. Structures in migmatite: a) Metaxitic amphibolite with a continuous network of leucosome veins concordant to discordant to the syn-migmatitic foliation; b) Metatexite with a texturally continuous network of leucosome veins delineating the syn-migmatitic foliation, isoclinal folds and shear zones; c) Asymmetric metatexite boudins in heterogeneous granite (or diatexite); d) Asymmetric synmigmatitic (viscous) folds; e) Texturally continuous network of leucosome veins delineating the syn-nmigmatitic foliation and a dextral shear zone; f) syn-migmatitic strike-slip fault; g) Metatexite raft with folded leucosome in textural continuity with the heterogeneous granite (or diatexite); h) texturally continuous network of leucosome veins delineating the syn-migmatitic foliation, folds and shear zones; i) Metatexite with syn-migmatitic foliation marked by concordant leucosome in textural continuity with discordant leucosome localized in shear zones.

Figure 8. Projection of field measurements of structural elements onto the lower hemisphere of a Schmidt diagram.

Figure 9. Deformation in granitoids and mylonite: a) asymmetric boudins; b-c) granitic veins in shear zones associated with asymmetric folds; d) folded quartz veins with boudinaged hinges; e) quartz tension gashes; f) synfolial F_{n+2} folds; g) M-shaped F_{n+3} folds in ultramylonite; h) S-shaped F_{n+3} folds in ultramylonite; i-j) Z-shaped F_{n+2} folds.

Figure 10. a) MgO vs. Zr diagram; b) Nb/Y vs. Zr/TiO_2 diagram; c) AFM diagram (Irvine and Baragar, 1971); d) A/CNK-A/Nk diagram (Shand, 1943); e) Log (SiO_2/ Al_2O_3) vs. Log (Fe_2O_3/ K_2O) diagram (Herron, 1988); f) sediment provenance characterisation (Roser and Korsch, 1988); g) A-CN-K diagram (Nesbitt and Young, 1989).

Figure 11. Primitive mantle-normalized multi-elements diagrams (values from McDonough and Sun, 1995) and Chondrite-normalized REE patterns (values from Anders and Grevesse, 1989).

Figure 12. Classification of granitoids: a) TAS diagram (Cox et al., 1979); b) SiO_2-K_2O diagram (Peccerillo and Taylor, 1976); c and d) MALI diagram (Frost et al., 2001).

Figure 13. Harker diagram for selected oxides (wt. %) and trace elements (ppm) in granitoids.

Figure 14. Evolutionary process discrimination diagram: a) La vs. La/Yb; b) Zr vs. Zr/Nb; c) La vs. La/Sm.

Figure 15. Mg# vs. SiO_2 diagram.

Table 1. Whole rock geochemical data for amphibolite, metapyroxenite, migmatite and paragneiss.

Rocks	Amphibolite			Metapyroxenite	Migmatite	Gneisses		
Samples	GN7	NGN5	NGN3	OUN2	GN3	TN1	TN2	GN6
wt%								
SiO_2	54.80	43.96	52.11	43.76	72.22	71.83	73.95	53.65
Al_2O_3	15.68	15.31	14.95	16.73	10.01	12.58	11.59	18.22
Fe_2O_3	9.61	14.32	7.45	12.26	7.10	4.76	4.62	9.23
MnO	0.14	0.31	0.18	0.18	0.11	0.09	0.07	0.10
MgO	5.19	7.36	6.81	7.07	1.91	1.52	1.45	3.85
CaO	6.46	9.08	6.88	9.24	1.41	2.47	2.11	6.61
Na_2O	0.62	2.63	2.76	2.95	2.00	3.20	3.16	0.88
K_2O	3.41	2.52	5.04	2.55	3.13	1.72	1.64	3.48
TiO_2	1.34	1.96	1.07	1.59	0.98	0.63	0.55	1.26
P_2O_5	0.62	0.17	0.63	0.85	< L.D.	0.17	0.13	0.55
LOI	0.97	1.19	1.27	1.49	0.48	0.89	0.74	0.98
Total	98.83	98.80	99.15	98.66	99.35	99.85	100.01	98.80
FeOt	8.65	12.89	6.70	11.03	6.39	4.28	4.16	8.31
Mg#	51.69	50.45	64.42	53.33	34.77	38.75	38.34	45.25
A/CNK	0.95	0.65	0.66	0.69	1.08	1.08	1.07	1.06
A/NK	3.33	2.17	1.50	2.20	1.50	1.77	1.66	3.49
ppm								
As	< L.D.	< L.D.	< L.D.	0.78	< L.D.	< L.D.	< L.D.	< L.D.
Ba	1367	104	2071	2439	271	137	116	1635
Be	3.45	3.44	2.50	1.56	2.09	2.97	2.76	2.68
Bi	0.09	0.30	0.11	0.15	< L.D.	0.07	0.05	0.05
Cd	0.12	0.58	0.28	0.20	0.06	0.04	0.04	0.05
Co	30.7	50.1	30.9	43.5	13.7	9.93	9.99	22.7
Cr	261	255	434	58.7	323	136	266	206
Cs	7.48	7.43	4.24	2.40	10.0	5.54	5.16	10.5
Cu	14.0	19.2	< L.D.	41.0	3.0	14.0	10.9	11.8
Ga	25.1	24.1	22.0	22.2	20.1	17.9	15.3	25.1
Ge	1.89	2.32	1.57	1.65	1.40	1.52	1.60	1.42
Hf	3.69	3.50	3.82	4.15	10.5	5.46	5.47	4.34
In	0.12	0.19	0.06	0.08	0.05	0.08	0.07	0.05
Mo	13.8	1.40	1.50	1.47	18.5	5.45	13.6	10.4
Nb	10.5	4.83	12.0	6.03	9.13	12.5	10.4	8.32
Ni	23.6	75.7	136	29.1	30.9	17.4	17.6	12.8
Pb	6.83	8.00	20.7	8.46	13.3	12.8	12.4	8.29
Rb	238	179	207	91.9	242	198	186	243
Sb	0.10	0.08	0.07	0.19	0.08	0.08	0.09	0.08
Sc	27.14	47.57	18.33	33.96	15.01	10.73	10.07	19.16
Sn	2.62	8.22	3.28	1.60	1.30	2.55	2.61	1.29
Sr	658	115	507	1259	102	161	148	777
Ta	1.12	0.44	0.71	0.33	0.12	1.00	0.95	0.71
Th	8.84	2.29	7.17	2.24	33.7	12.3	10.8	13.0
U	3.44	1.31	2.09	0.50	56.6	3.74	4.17	2.24
V	210	305	152	258	104	68.8	59.5	171
W	10.7	70.6	1.06	1.16	12.6	4.63	14.1	9.17
Y	31.2	48.9	20.7	30.8	5.20	13.4	11.3	19.1
Zn	100	183	115	118	123	79.7	82.8	95.1
Zr	132	124	155	162	387	198	202	167
La	36.5	57.8	37.2	44.7	34.1	28.2	19.2	44.8
Ce	96.7	110	64.0	101	153	59.4	43.6	92.1
Pr	12.9	12.3	9.53	13.2	9.30	6.90	5.31	11.0
Nd	54.3	46.4	39.3	57.5	33.4	25.3	19.9	44.0
Sm	11.3	9.31	7.91	11.8	5.81	4.83	4.00	8.44
Eu	2.87	2.47	2.02	3.44	0.453	0.70	0.60	1.96
Gd	8.55	8.80	6.03	8.97	3.70	3.71	2.99	6.23
Tb	1.17	1.40	0.77	1.18	0.40	0.52	0.44	0.79
Dy	6.37	8.81	3.89	6.41	1.63	2.86	2.42	4.18
Ho	1.19	1.87	0.69	1.20	0.23	0.54	0.45	0.76
Er	3.06	5.00	1.67	2.99	0.511	1.37	1.16	1.85
Tm	0.45	0.74	0.23	0.41	0.07	0.19	0.16	0.25
Yb	2.91	4.66	1.37	2.51	0.54	1.23	0.998	1.54
Lu	0.42	0.70	0.21	0.36	0.09	0.19	0.15	0.22
ΣREE	238.69	270.27	174.81	255.67	243.24	135.94	101.38	218.12
Eu/Eu*	0.89	0.83	0.89	1.02	0.3	0.5	0.53	0.82
$(Ce/Sm)_N$	2.09	2.88	1.97	2.09	6.42	3	2.66	2.66
$(Gd/Yb)_N$	2.43	1.56	3.64	2.95	5.67	2.49	2.48	3.34
$(La/Yb)_N$	8.68	8.59	18.8	12.33	43.72	15.87	13.32	20.14

1298 **Table 2:** Whole rock geochemical data for granitoids.

Rocks	Tonalite	Granodiorite		Heterogeneous granite								
				Monzogranite					Syenogranite			Alk. Felds. Gr
Samples	MOL1	TME1	OUN3	NGN1	NG03b	KN1	KNY3	KNY2	BDN2	NG03a	MAN1	GN2
wt%												
SiO_2	62.21	64.05	70.54	72.34	71.49	72.20	73.53	74.57	76.35	71.21	79.47	69.80
Al_2O_3	16.26	16.62	14.61	13.95	14.16	13.37	13.84	12.89	12.86	14.28	11.41	14.18
Fe_2O_3	5.59	4.72	2.87	1.73	2.36	2.61	2.23	2.04	0.89	1.63	0.88	2.38
MnO	0.068	0.092	0.068	0.030	0.037	0.039	0.055	0.036	NA	0.027	0.026	0.038
MgO	2.69	1.58	0.77	0.52	0.67	0.53	0.36	0.30	0.07	0.42	0.06	0.46
CaO	3.52	3.93	2.28	1.87	1.82	1.49	1.74	1.34	1.01	1.42	0.49	0.93
Na_2O	4.30	4.31	3.90	3.13	3.31	3.37	3.57	3.21	2.47	3.14	3.63	2.57
K_2O	2.50	3.11	3.71	5.06	4.84	4.52	4.48	4.69	6.08	5.97	4.02	7.17
TiO_2	1.15	0.67	0.40	0.27	0.26	0.28	0.23	0.20	0.063	0.18	0.10	0.52
P_2O_5	0.32	0.21	0.13	NA	0.10	NA	NA	NA	NA	NA	NA	0.16
LOI	0.79	0.46	0.45	0.48	0.46	0.59	0.40	0.22	0.37	0.59	0.14	0.51
Total	99.38	99.74	99.72	99.39	99.50	99.01	100.43	99.49	100.16	98.86	100.23	98.72
FeOt	5.03	4.25	2.58	1.56	2.12	2.35	2.01	1.84	0.80	1.47	0.79	2.14
Mg#	48.81	39.87	34.71	37.32	36.00	28.69	24.23	22.56	13.48	33.80	11.90	27.69
A/CNK	1.00	0.94	1.00	0.99	1.01	1.02	1.00	1.01	1.03	1.00	1.02	1.04
A/NK	1.66	1.59	1.40	1.31	1.33	1.28	1.29	1.24	1.21	1.23	1.11	1.18
ppm												
As	< L.D.	< L.D.	< L.D.	< L.D.	< L.D.	< L.D.	< L.D.	< L.D.	< L.D.	0.51	< L.D.	< L.D.
Ba	303	1198	605	772	803	496	644	459	470	765	59.7	902
Be	3.48	2.52	2.28	2.79	2.97	2.84	2.39	2.10	1.64	2.66	0.90	1.74
Bi	0.14	< L.D.	0.06	0.05	0.06	< L.D.	< L.D.	< L.D.	< L.D.	< L.D.	< L.D.	0.05
Cd	0.03	0.08	0.03	0.04	0.03	0.02	0.09	0.05	< L.D.	0.04	< L.D.	0.05
Co	15.8	9.08	3.86	3.37	3.74	3.15	2.40	1.30	0.87	2.84	0.39	2.79
Cr	95.9	79.1	54.2	126	104	90.3	141	78.6	103	146	185	114
Cs	7.83	1.04	3.73	2.89	4.90	1.98	3.91	4.61	2.37	3.19	0.22	3.76
Cu	4.7	9.6	3.4	8.3	< L.D.	< L.D.	< L.D.	5.6	8.4	< L.D.	< L.D.	3.8
Ga	26.5	21.8	18.2	18.3	19.7	21.4	16.5	15.5	14.4	19.4	15.0	19.4
Ge	1.15	1.36	1.27	1.15	1.07	1.23	1.66	1.27	1.05	1.17	1.37	1.33
Hf	2.83	6.52	4.14	3.08	4.61	4.76	3.69	4.45	3.20	4.68	3.26	8.86
In	< L.D.	0.05	< L.D.	< L.D.	< L.D.	< L.D.	0.05	< L.D.	< L.D.	< L.D.	< L.D.	< L.D.
Mo	3.88	4.77	3.52	8.52	5.72	4.91	8.76	5.52	6.45	8.64	11.3	9.05
Nb	13.0	11.9	7.33	9.10	3.76	7.16	9.89	9.43	1.76	4.50	5.17	8.76
Ni	17.7	4.6	< L.D.	25.1	4.1	3.2	2.2	< L.D.	< L.D.	2.9	2.2	2.7
Pb	14.9	17.6	18.7	26.4	27.1	25.4	20.9	20.5	29.2	33.3	20.2	43.3
Rb	219	98.0	152	172	172	188	171	176	161	222	101	242
Sb	0.10	0.11	0.08	0.10	0.13	0.09	0.07	0.06	0.14	0.09	0.08	0.09
Sc	2.56	10.41	7.77	3.05	4.88	3.59	4.84	2.62	< L.D.	2.43	1.31	5.24
Sn	2.97	3.13	1.74	2.82	1.42	2.41	2.09	1.42	0.51	1.67	0.69	0.53
Sr	492	467	178	222	205	170	109	82.3	170	229	23.0	203
Ta	1.32	1.14	0.40	1.43	0.15	0.31	0.61	0.44	0.44	0.64	0.28	0.16
Th	19.2	5.30	5.13	10.4	2.64	21.3	12.8	19.6	6.67	40.3	26.8	36.9
U	2.22	0.63	1.19	1.86	1.16	1.68	1.42	2.04	2.49	5.01	1.41	2.35
V	92.3	72.4	27.1	21.9	29.2	32.4	15.1	11.8	7.7	22.6	5.0	24.5
W	3.12	3.83	2.91	5.48	4.97	4.29	7.57	4.26	5.66	7.31	9.78	5.96
Y	9.29	36.0	20.2	19.1	3.47	9.95	23.4	14.4	3.67	17.2	3.59	5.48
Zn	100	75.3	64.7	31.0	43.4	43.6	40.0	32.1	< L.D.	30.0	14.6	34.1
Zr	104	235	143	101	148	152	122	143	75.8	157	80.9	323
La	37.1	32.2	20.5	19.9	7.46	37.6	29.6	9.94	3.72	35.1	24.5	65.7
Ce	91.2	83.0	43.7	41.1	10.5	72.6	58.5	18.6	4.35	57.9	43.6	191
Pr	7.37	10.3	5.11	5.00	1.10	7.42	6.38	2.37	0.514	5.66	4.07	15.8
Nd	24.8	40.2	19.6	19.8	4.08	24.8	23.0	9.51	1.75	18.6	11.8	54.1
Sm	3.76	8.10	4.64	4.75	0.790	4.35	4.65	2.24	0.332	3.41	1.63	8.40
Eu	1.17	1.46	0.908	1.01	0.524	0.718	0.855	0.630	0.733	0.660	0.260	1.41
Gd	2.47	6.53	4.29	3.99	0.697	3.01	4.04	2.26	0.298	2.77	1.14	4.30
Tb	0.315	1.03	0.664	0.629	0.091	0.401	0.659	0.386	0.059	0.418	0.132	0.406
Dy	1.73	6.33	3.91	3.76	0.518	2.15	4.18	2.45	0.450	2.43	0.656	1.62
Ho	0.330	1.31	0.772	0.732	0.114	0.393	0.875	0.522	0.116	0.478	0.120	0.238
Er	0.930	3.56	1.96	1.93	0.326	0.927	2.39	1.42	0.398	1.29	0.315	0.572
Tm	0.150	0.546	0.268	0.291	0.0525	0.116	0.355	0.208	0.0801	0.192	0.0445	0.0758
Yb	1.07	3.49	1.60	1.85	0.407	0.670	2.23	1.28	0.637	1.16	0.326	0.564
Lu	0.173	0.490	0.227	0.256	0.075	0.099	0.322	0.194	0.108	0.166	0.057	0.089
ΣREE	172.57	198.55	108.15	105	26.73	155.25	138.04	52.01	13.55	130.23	88.65	344.27
Eu/Eu*	1.17	0.61	0.62	0.7	2.14	0.6	0.6	0.85	7.08	0.65	0.58	0.71
$(Ce/Sm)_N$	5.92	2.5	2.3	2.11	3.24	4.07	3.07	2.02	3.2	4.14	6.52	5.55
$(Gd/Yb)_N$	1.91	1.55	2.22	1.78	1.42	3.72	1.5	1.46	0.39	1.97	2.89	6.3
$(La/Yb)_N$	24.01	6.39	8.87	7.45	12.69	38.86	9.19	5.38	4.04	20.95	52.03	80.65

1299 **Table 3.** Whole rock Sr-Nd isotopes

	Amphibolite		Heterogeneous granite	
Samples	NGN5	OUN2	NG03b	BDN2
Rb (ppm)	178.6329	91.8515	172.3067	160.7674
Sr (ppm)	115.0961	1259.3279	205.1082	170.0765
$^{87}Sr/^{86}Sr$	0.746290	0.709418	0.731975	0.735422
$^{87}Rb/^{86}Sr$	4.5220837	0.2113048	2.4341736	2.7485271
2σ	0.000016	0.000016	0.000008	0.000016
$^{87}Sr/^{86}Sr_{610}$	0.706950	0.707580	0.710799	0.711511
$^{87}Sr/^{86}Sr_{654}$	0.704034	0.707443	0.709229	0.709739
Nd (ppm)	46.43	57.54	4.08	1.75
Sm (ppm)	9.31	11.84	0.79	0.33
$^{143}Nd/^{144}Nd$	0.512057	0.512089	0.511804	0.511871
$^{147}Sm/^{144}Nd$	0.1212885	0.1240525	0.1170386	0.114675
2σ	6.10E-06	8.10E-06	8.10E-06	7.10E-06
$^{143}Nd/^{144}Nd_{610}$	0.511572	0.511593	0.511336	0.511413
εNd_{610}	-5.46	-5.05	-10.07	-8.58
$^{143}Nd/^{144}Nd_{655}$	0.511536	0.511556	0.511302	0.511379
εNd_{654}	-5.03	-4.63	-9.61	-8.11
εNd_0	-11.33	-10.71	-16.27	-14.96
T_{DM} (Ga)	1.702	1.701	2.01	1.87

1300

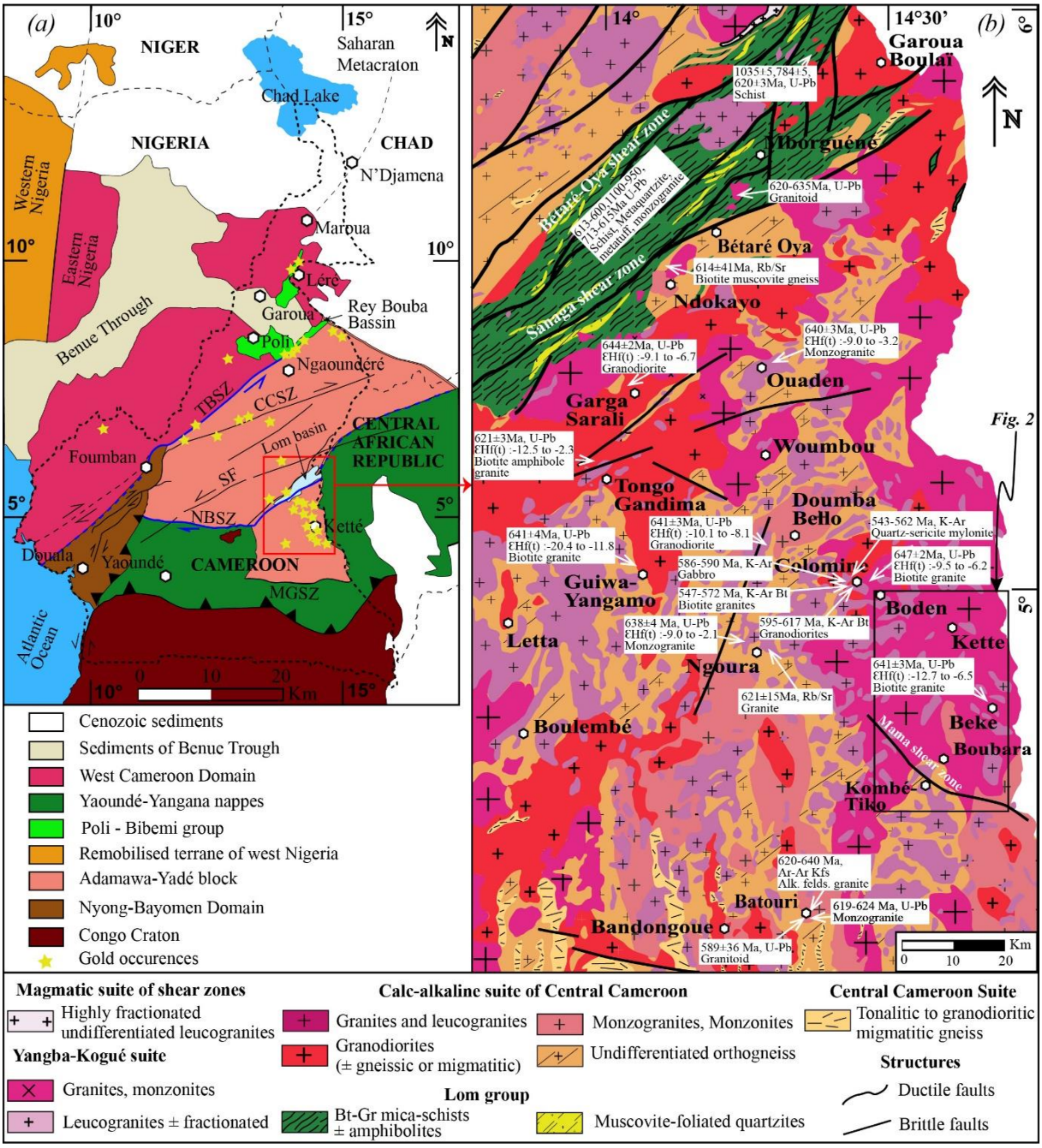
(a)
NIGER
NIGERIA
CHAD
Saharan Metacraton
Chad Lake
N'Djamena
Maroua
Lere
Garoua
Rey Bouba Bassin
Poli
Ngaoundéré
Benue Through
Western Nigeria
Eastern Nigeria
TBSZ
CCSZ
Lom basin
SF
NBSZ
CENTRAL AFRICAN REPUBLIC
Foumban
Douala
Yaoundé
CAMEROON
MGSZ
Ketté
Atlantic Ocean
Km
(b)
Garoua Boulaï
Mborguéné
Bétaré Oya
Ndokayo
Ouaden
Garga Sarali
Woumbou
Tongo Gandima
Doumba Bello
Guiwa-Yangamo
Letta
Ngoura
Boulembé
Boden
Kette
Beke Boubara
Kombé-Tiko
Batouri
Bandongoue
Fig. 2
Bétaré-Oya shear zone
Sanaga shear zone
Mama shear zone
1035±5,784±5, 620±3Ma, U-Pb Schist
620-635Ma, U-Pb Granitoid
614±41Ma, Rb/Sr Biotite muscovite gneiss
640±3Ma, U-Pb εHf(t) :-9.0 to -3.2 Monzogranite
644±2Ma, U-Pb εHf(t) :-9.1 to -6.7 Granodiorite
621±3Ma, U-Pb εHf(t) :-12.5 to -2.3 Biotite amphibole granite
641±3Ma, U-Pb εHf(t) :-10.1 to -8.1 Granodiorite
641±4Ma, U-Pb εHf(t) :-20.4 to -11.8 Biotite granite
543-562 Ma, K-Ar Quartz-sericite mylonite
647±2Ma, U-Pb εHf(t) :-9.5 to -6.2 Biotite granite
586-590 Ma, K-Ar Gabbro
547-572 Ma, K-Ar Bt Biotite granites
638±4 Ma, U-Pb εHf(t) :-9.0 to -2.1 Monzogranite
595-617 Ma, K-Ar Bt Granodiorites
641±3Ma, U-Pb εHf(t) :-12.7 to -6.5 Biotite granite
621±15Ma, Rb/Sr Granite
620-640 Ma, Ar-Ar Kfs Alk. felds. granite
619-624 Ma, U-Pb Monzogranite
589±36 Ma, U-Pb Granitoid
Cenozoic sediments
Sediments of Benue Trough
West Cameroon Domain
Yaoundé-Yangana nappes
Poli - Bibemi group
Remobilised terrane of west Nigeria
Adamawa-Yadé block
Nyong-Bayomen Domain
Congo Craton
Gold occurences
Magmatic suite of shear zones
Highly fractionated undifferentiated leucogranites
Yangba-Kogué suite
Granites, monzonites
Leucogranites ± fractionated
Calc-alkaline suite of Central Cameroon
Granites and leucogranites
Granodiorites (± gneissic or migmatitic)
Lom group
Bt-Gr mica-schists ± amphibolites
Monzogranites, Monzonites
Undifferentiated orthogneiss
Muscovite-foliated quartzites
Central Cameroon Suite
Tonalitic to granodioritic migmatitic gneiss
Structures
Ductile faults
Brittle faults

Figure 1

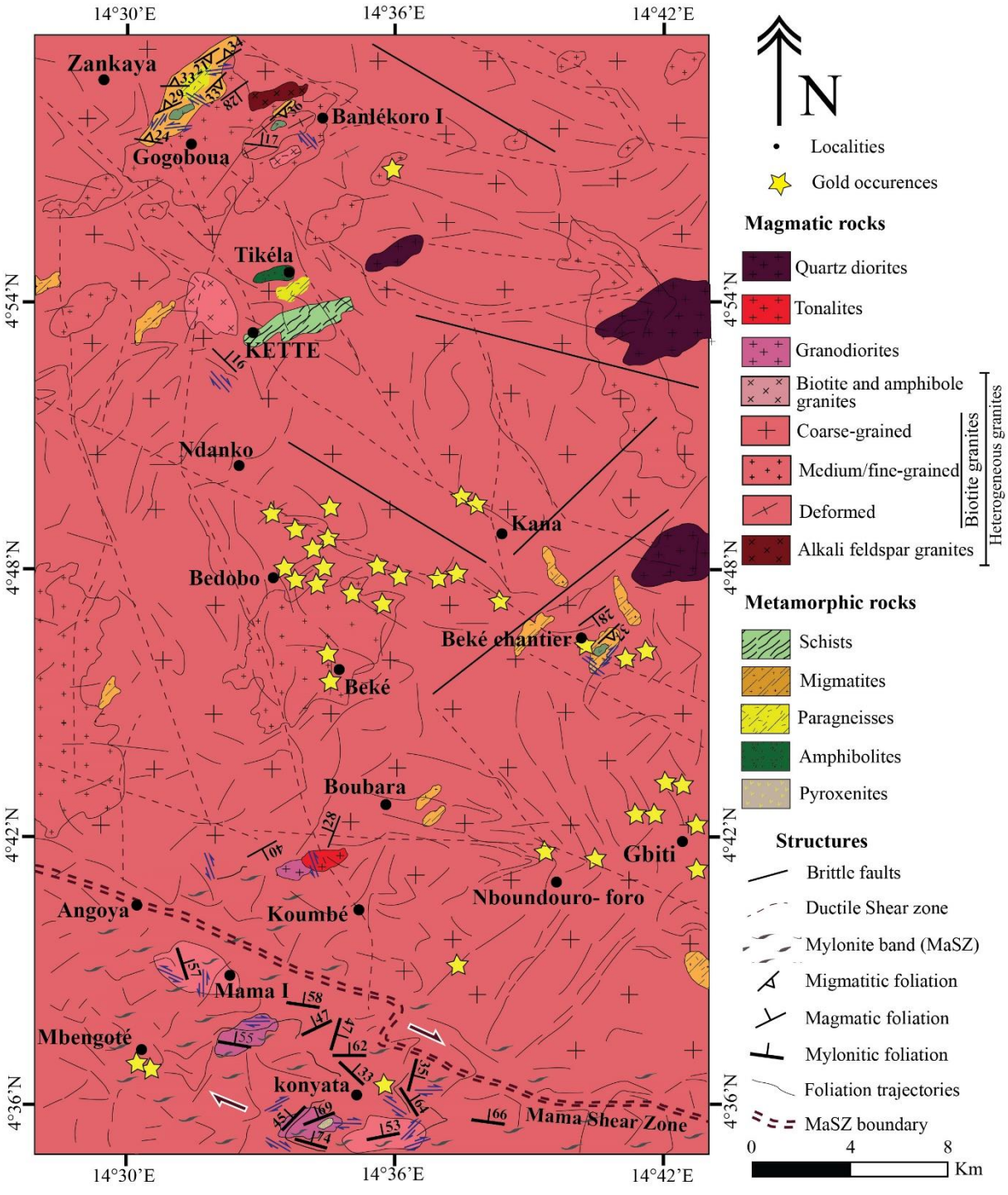

1303

1304 **Figure 2**

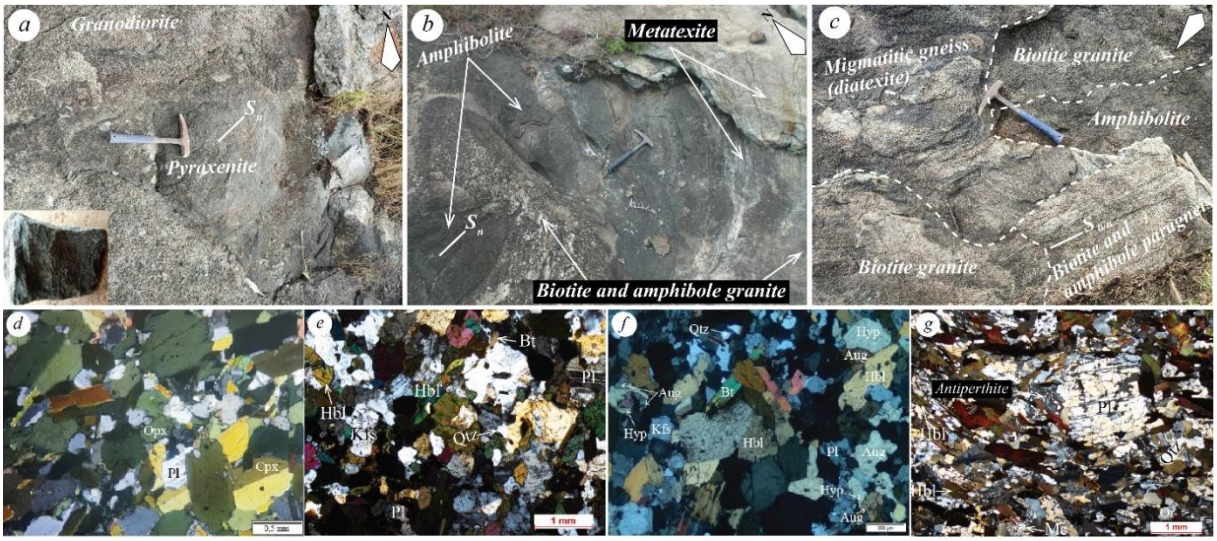

1305

1306 **Figure 3**

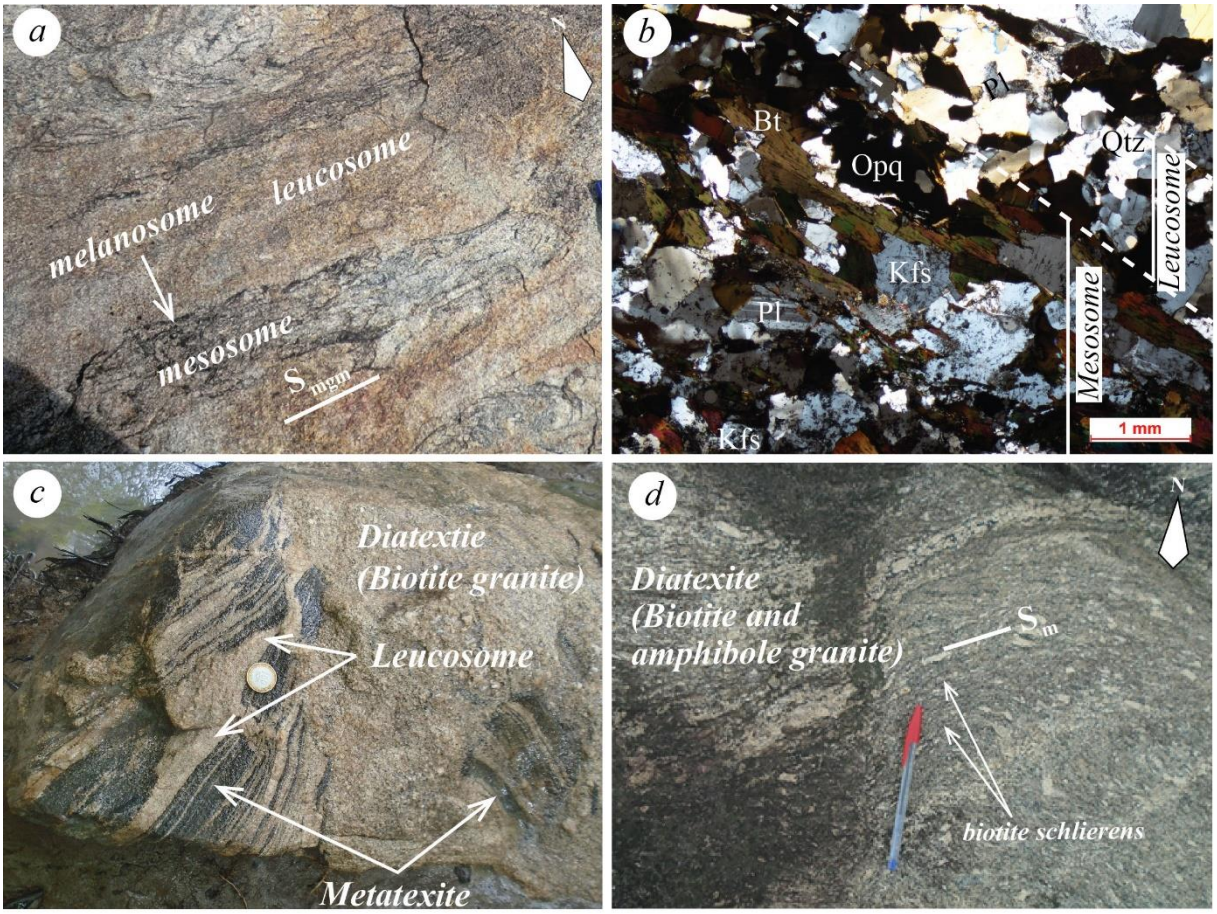

1307

1308 **Figure 4**

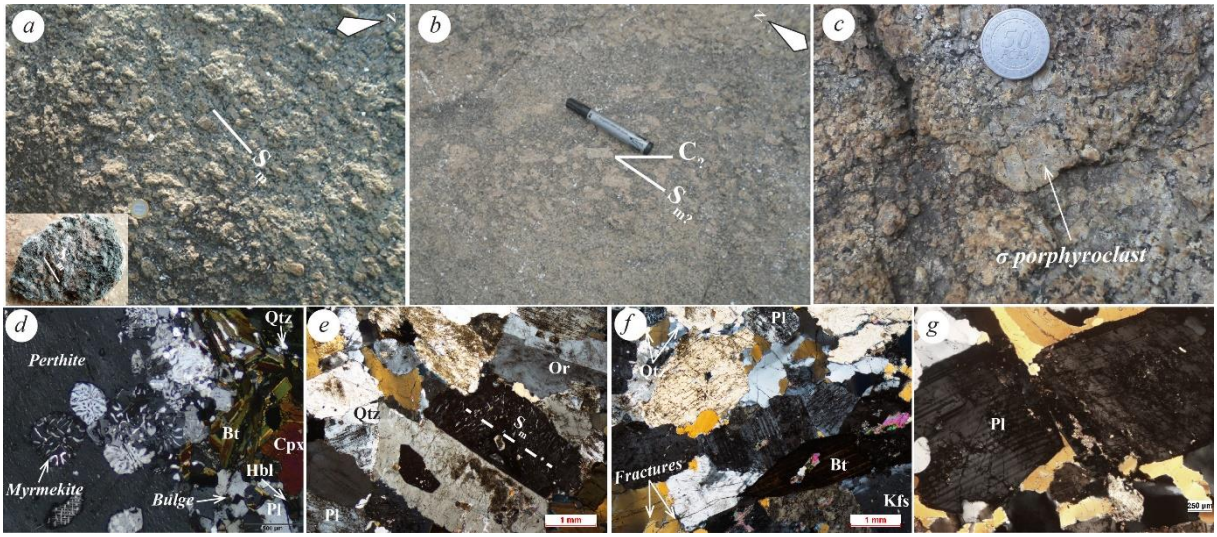
a
N
S_{m1}
b
N
C_{m1}
S_{m2}
c
σ porphyroclast
d
Qtz
Perthite
Bt
Cpx
Hbl
Myrmekite
Bulge
Pl
e
Or
Qtz
S_{m1}
Pl
1 mm
f
Pl
Qtz
Fractures
Bt
Kfs
1 mm
g
Pl
250 µm

Figure 5

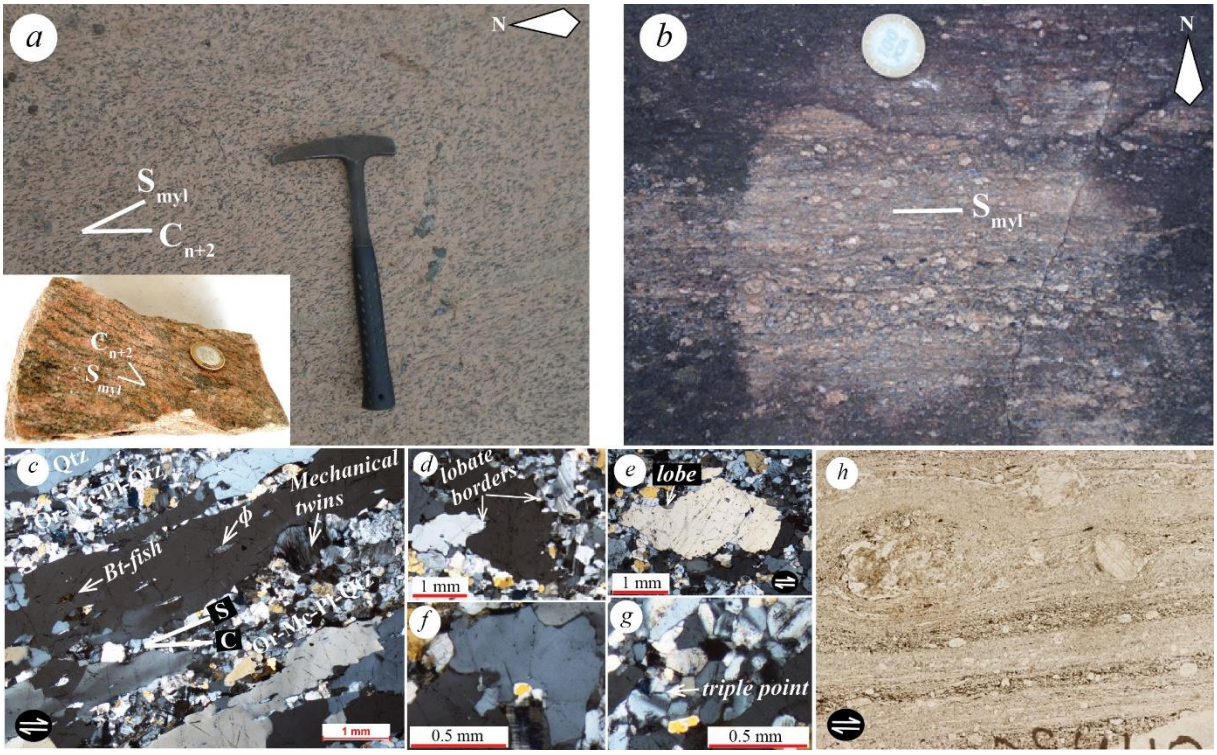
a
N
S myl
C n+2
C n+2
S myl
b
N
S myl
c
Qtz
Qtz
Mechanical twins
Bt-fish
S
C
1 mm
d
lobate borders
1 mm
e
lobe
1 mm
f
0.5 mm
g
triple point
0.5 mm
h

Figure 6

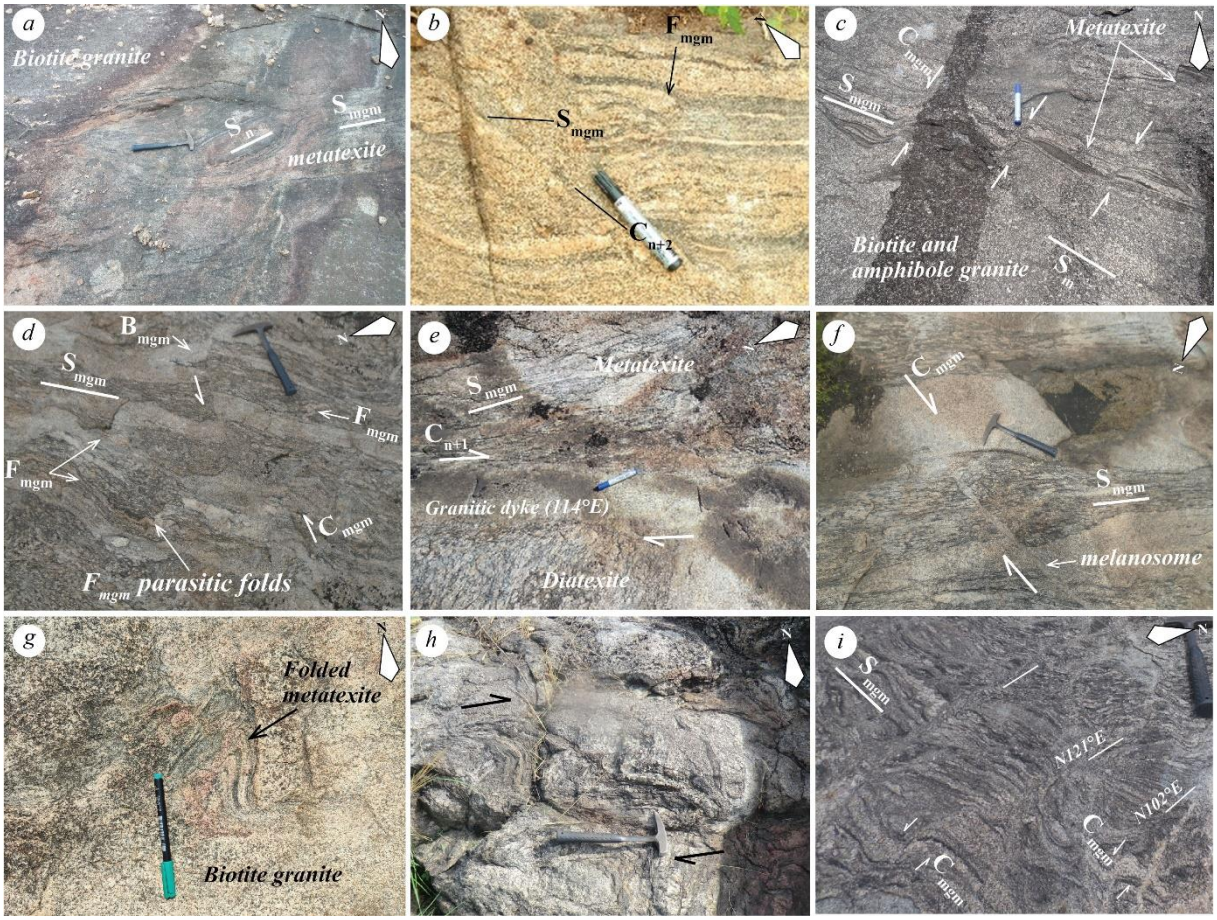

1313

1314 **Figure 7**

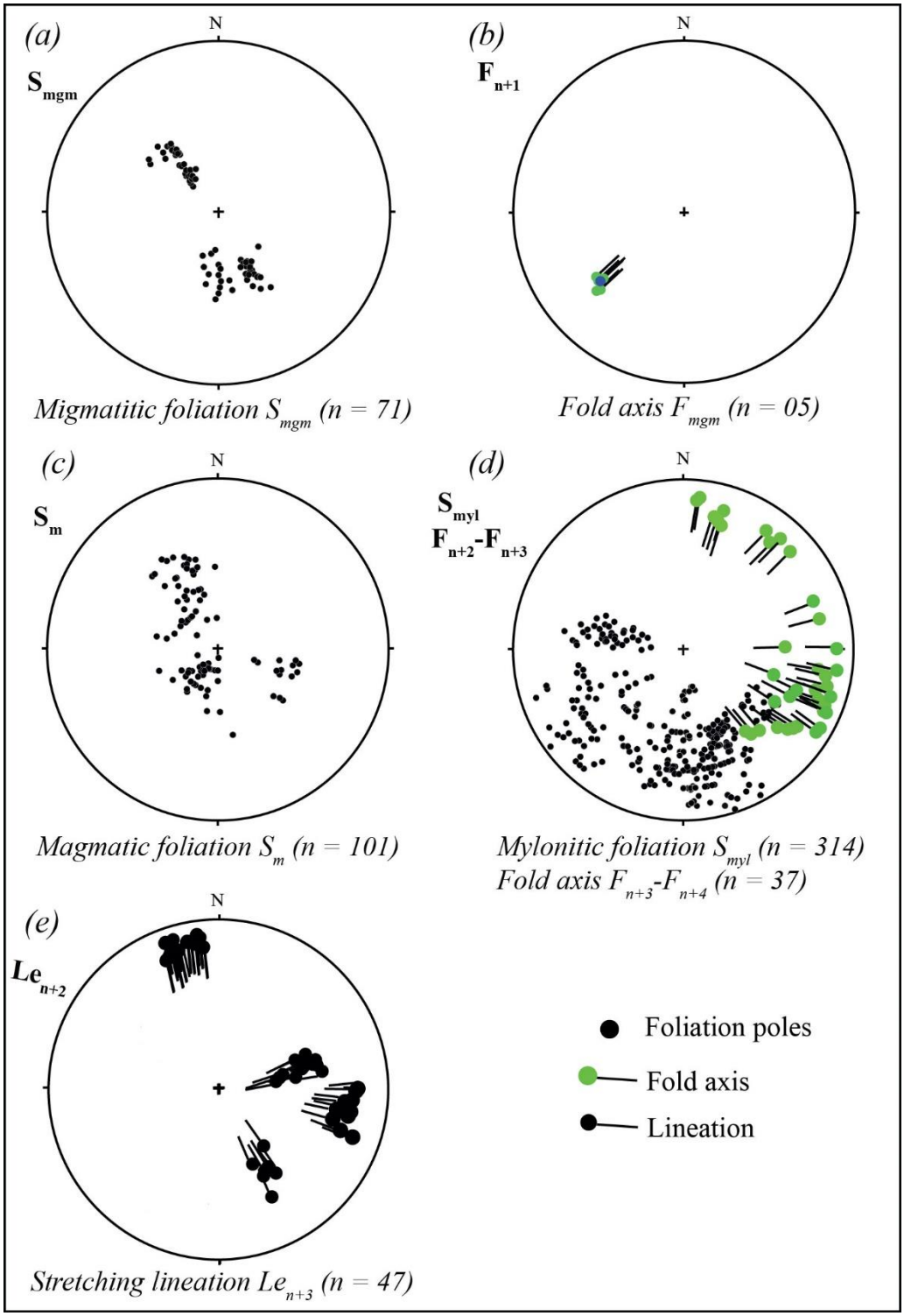

1315

1316 **Figure 8**

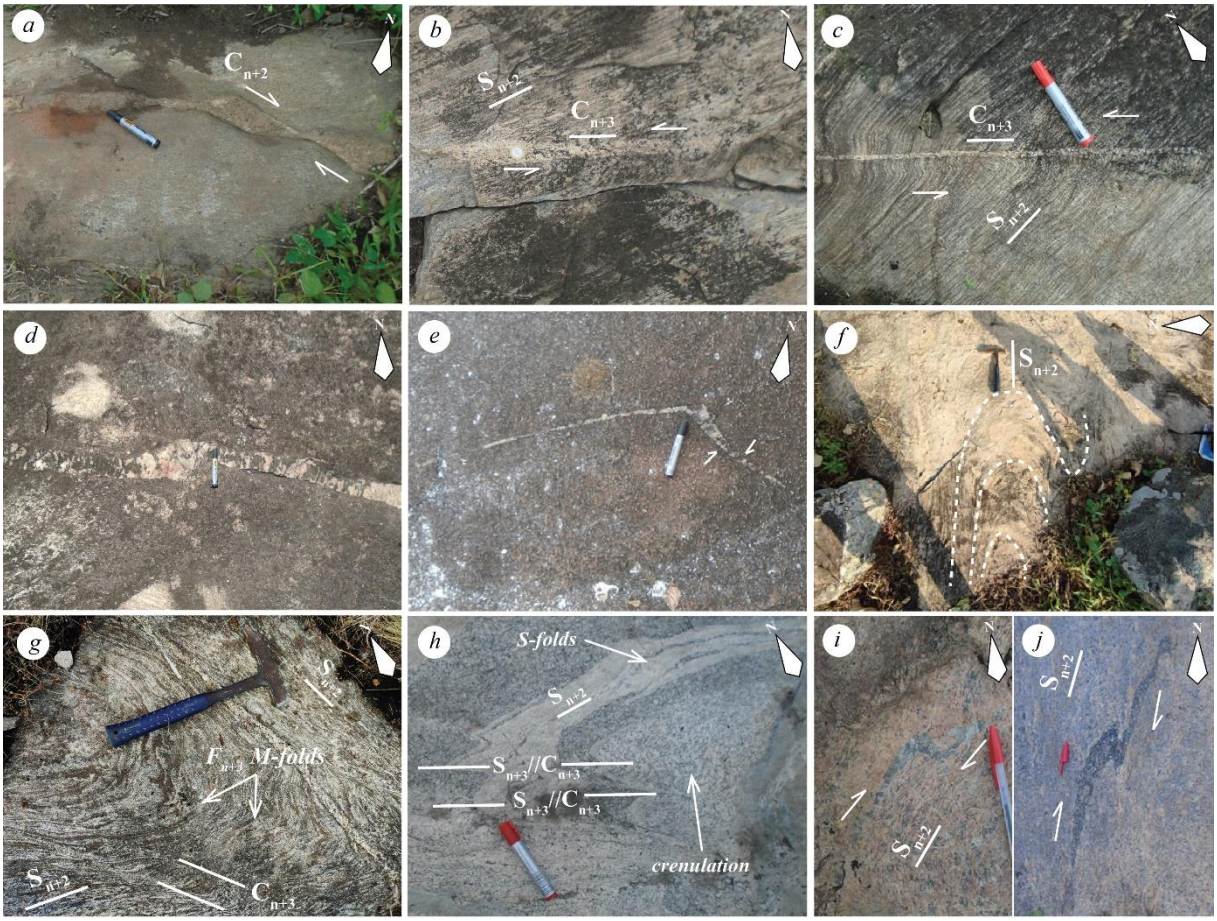
a
b
c
d
e
f
g
h
i
j
N
C_{n+2}
S_{n+2}
C_{n+3}
S_{n+2}
S_{n+2}
S_{n+2}
F_{n+3} M-folds
S_{n+2}
C_{n+3}
S-folds
S_{n+2}
S_{n+3}//C_{n+3}
S_{n+3}//C_{n+3}
crenulation
S_{n+2}
S_{n+2}

Figure 9

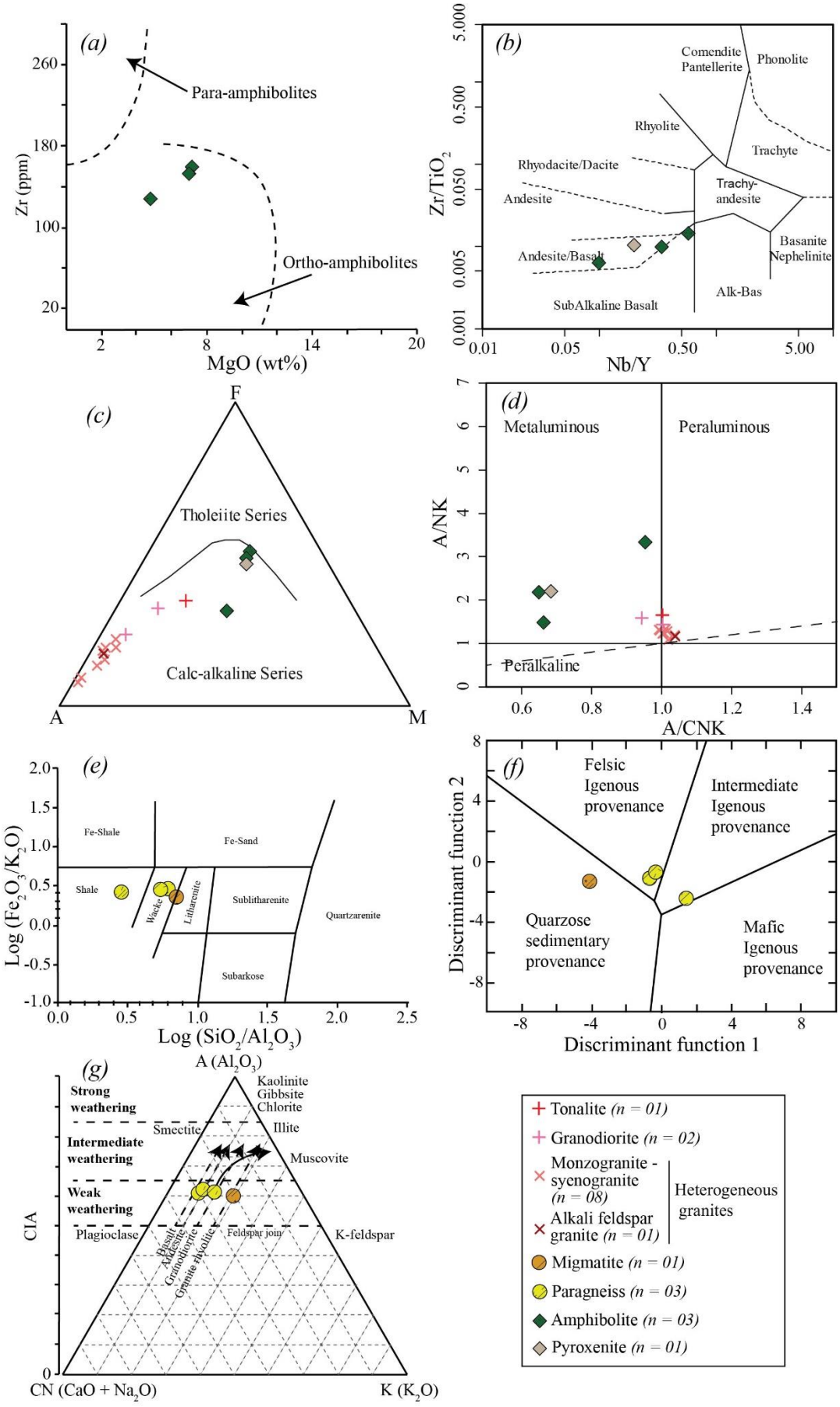
(a)
Para-amphibolites
Ortho-amphibolites
Zr (ppm)
MgO (wt%)
(b)
Comendite
Pantellerite
Phonolite
Rhyolite
Trachyte
Rhyodacite/Dacite
Trachy-
andesite
Andesite
Basanite
Nephelinite
Andesite/Basalt
Alk-Bas
SubAlkaline Basalt
Zr/TiO2
Nb/Y
(c)
F
Tholeiite Series
Calc-alkaline Series
A
M
(d)
Metaluminous
Peraluminous
Peralkaline
A/NK
A/CNK
(e)
Fe-Shale
Fe-Sand
Shale
Wacke
Litharenite
Sublitharenite
Quartzarenite
Subarkose
Log (Fe2O3/K2O)
Log (SiO2/Al2O3)
(f)
Felsic
Igenous
provenance
Intermediate
Igenous
provenance
Quarzose
sedimentary
provenance
Mafic
Igenous
provenance
Discriminant function 2
Discriminant function 1
(g)
A (Al2O3)
Strong
weathering
Intermediate
weathering
Weak
weathering
Kaolinite
Gibbsite
Chlorite
Smectite
Illite
Muscovite
Plagioclase
Feldspar join
K-feldspar
Basalt
Andesite
Granodiorite
Granite
Rhyolite
CIA
CN (CaO + Na2O)
K (K2O)
Tonalite (n = 01)
Granodiorite (n = 02)
Monzogranite - syenogranite (n = 08)
Alkali feldspar granite (n = 01)
Heterogeneous granites
Migmatite (n = 01)
Paragneiss (n = 03)
Amphibolite (n = 03)
Pyroxenite (n = 01)

Figure 10

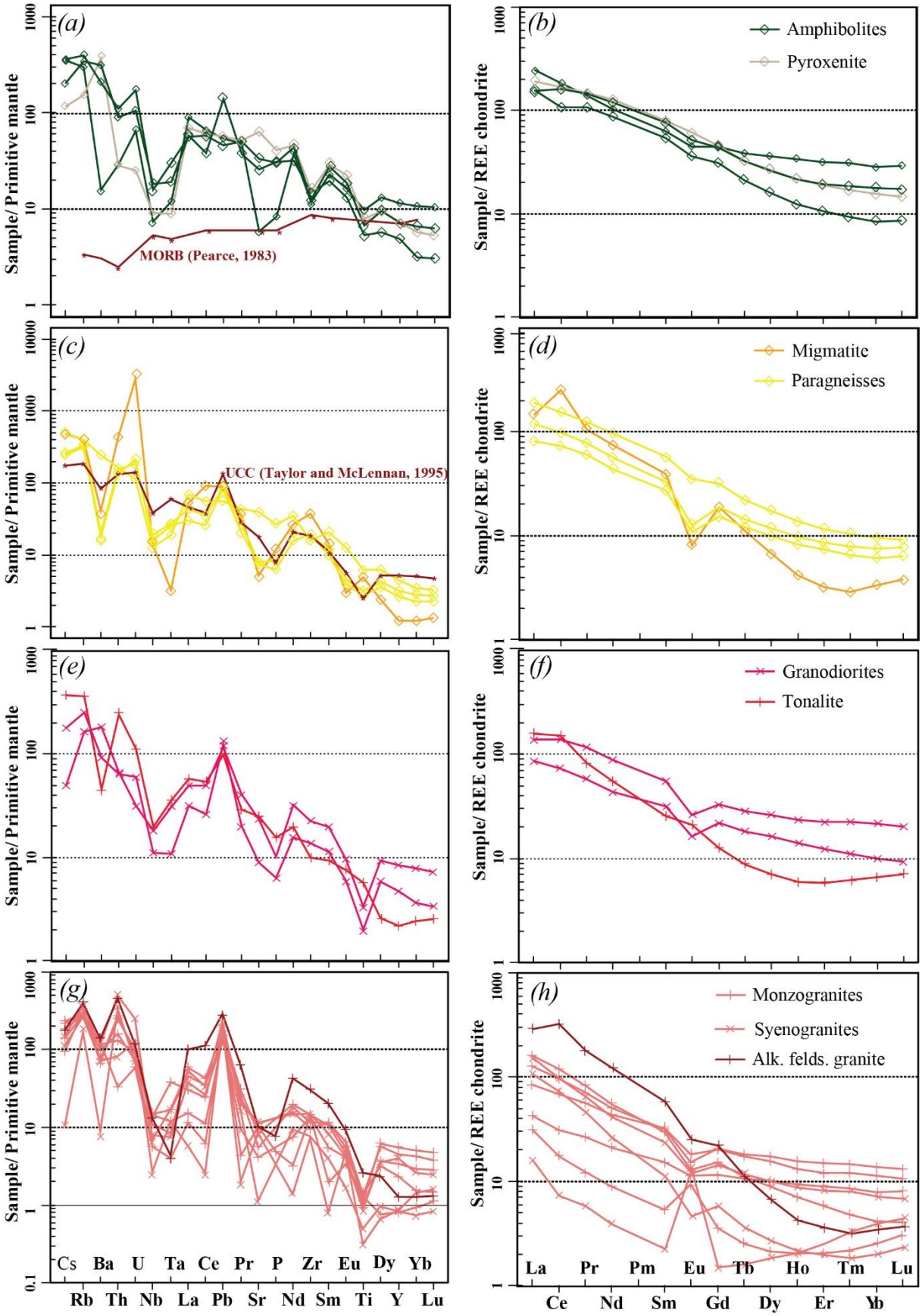
(a)
Sample/ Primitive mantle
MORB (Pearce, 1983)
(b)
Sample/ REE chondrite
Amphibolites
Pyroxenite
(c)
Sample/ Primitive mantle
UCC (Taylor and McLennan, 1995)
(d)
Sample/ REE chondrite
Migmatite
Paragneisses
(e)
Sample/ Primitive mantle
(f)
Sample/ REE chondrite
Granodiorites
Tonalite
(g)
Sample/ Primitive mantle
Cs Ba U Ta Ce Pr P Zr Eu Dy Yb
Rb Th Nb La Pb Sr Nd Sm Ti Y Lu
(h)
Sample/ REE chondrite
Monzogranites
Syenogranites
Alk. felds. granite
La Pr Pm Eu Tb Ho Tm Lu
Ce Nd Sm Gd Dy Er Yb

Figure 11

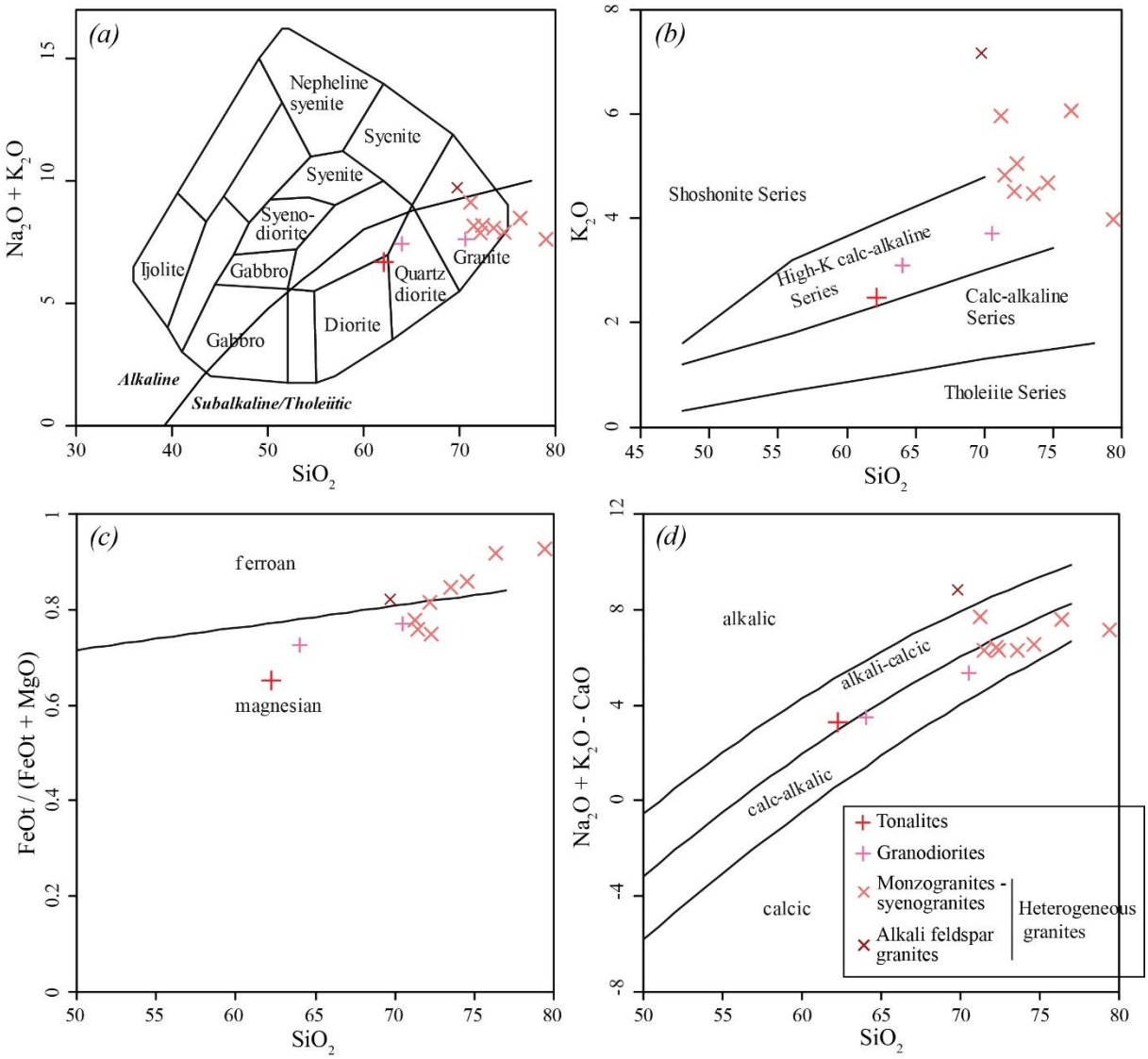
(a)
Nepheline syenite
Syenite
Syenite
Syeno-diorite
Ijolite
Gabbro
Quartz diorite
Granite
Diorite
Gabbro
Alkaline
Subalkaline/Tholeiitic
Na2O + K2O
SiO2
(b)
Shoshonite Series
High-K calc-alkaline Series
Calc-alkaline Series
Tholeiite Series
K2O
SiO2
(c)
ferroan
magnesian
FeOt / (FeOt + MgO)
SiO2
(d)
alkalic
alkali-calcic
calc-alkalic
calcic
Tonalites
Granodiorites
Monzogranites - syenogranites
Alkali feldspar granites
Heterogeneous granites
Na2O + K2O - CaO
SiO2

Figure 12

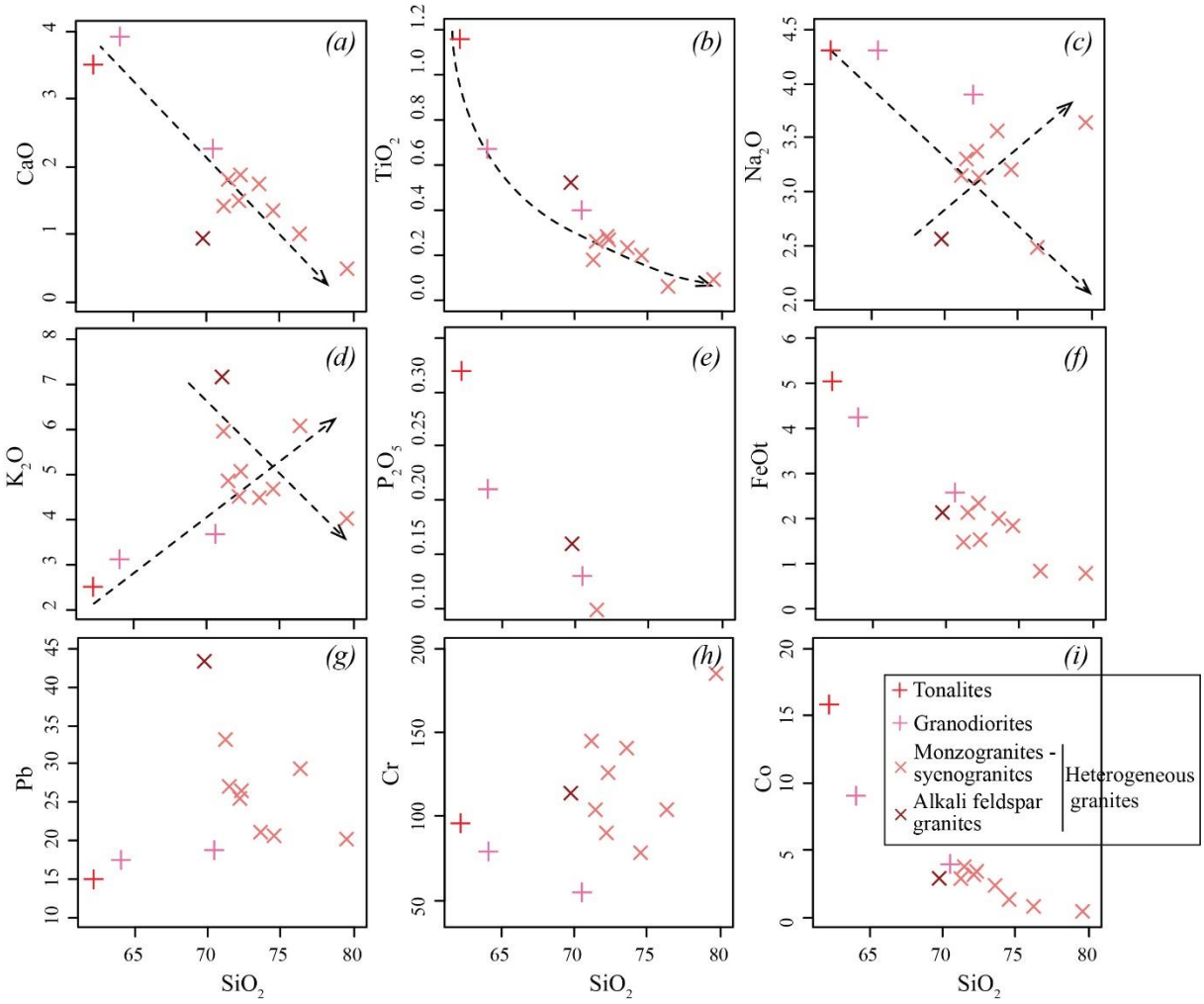
(a)
(b)
(c)
(d)
(e)
(f)
(g)
(h)
(i)
CaO
TiO2
Na2O
K2O
P2O5
FeOt
Pb
Cr
Co
SiO2
Tonalites
Granodiorites
Monzogranites - syenogranites
Alkali feldspar granites
Heterogeneous granites

Figure 13

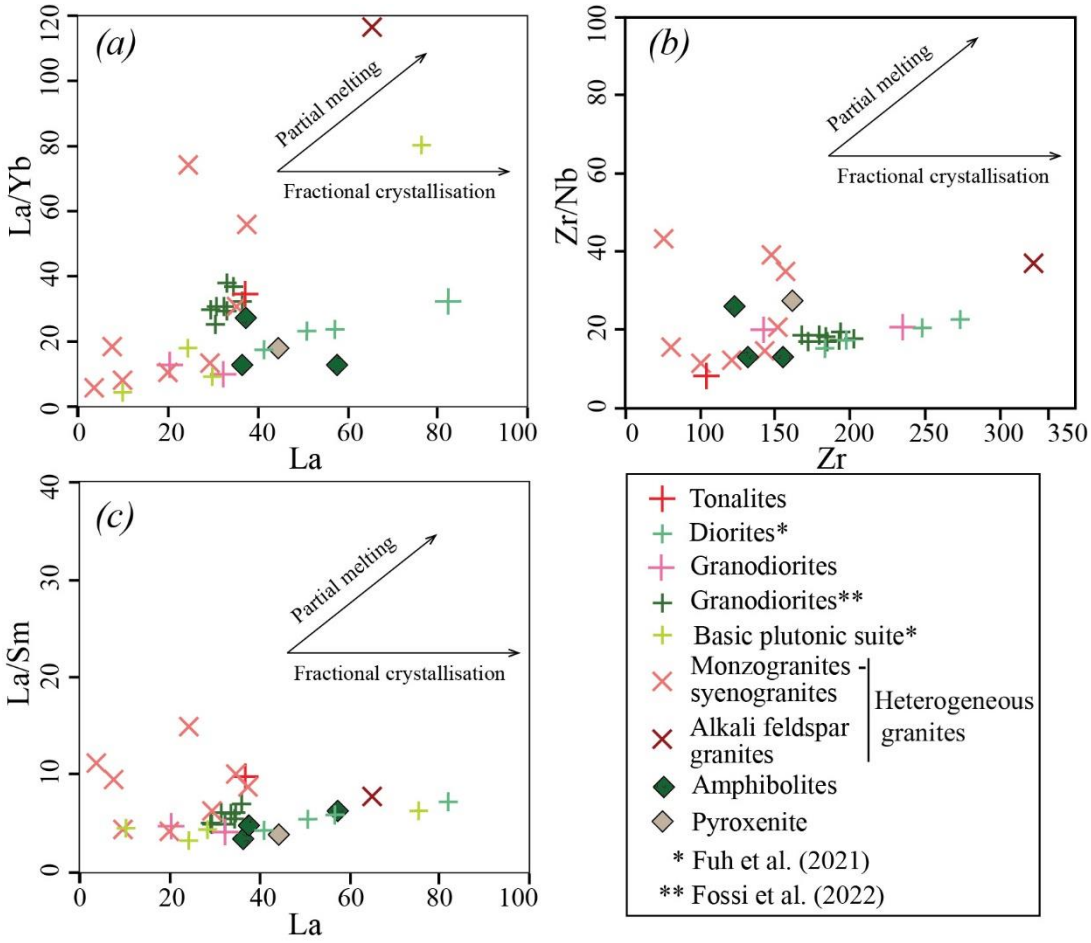

1327

1328 **Figure 14**

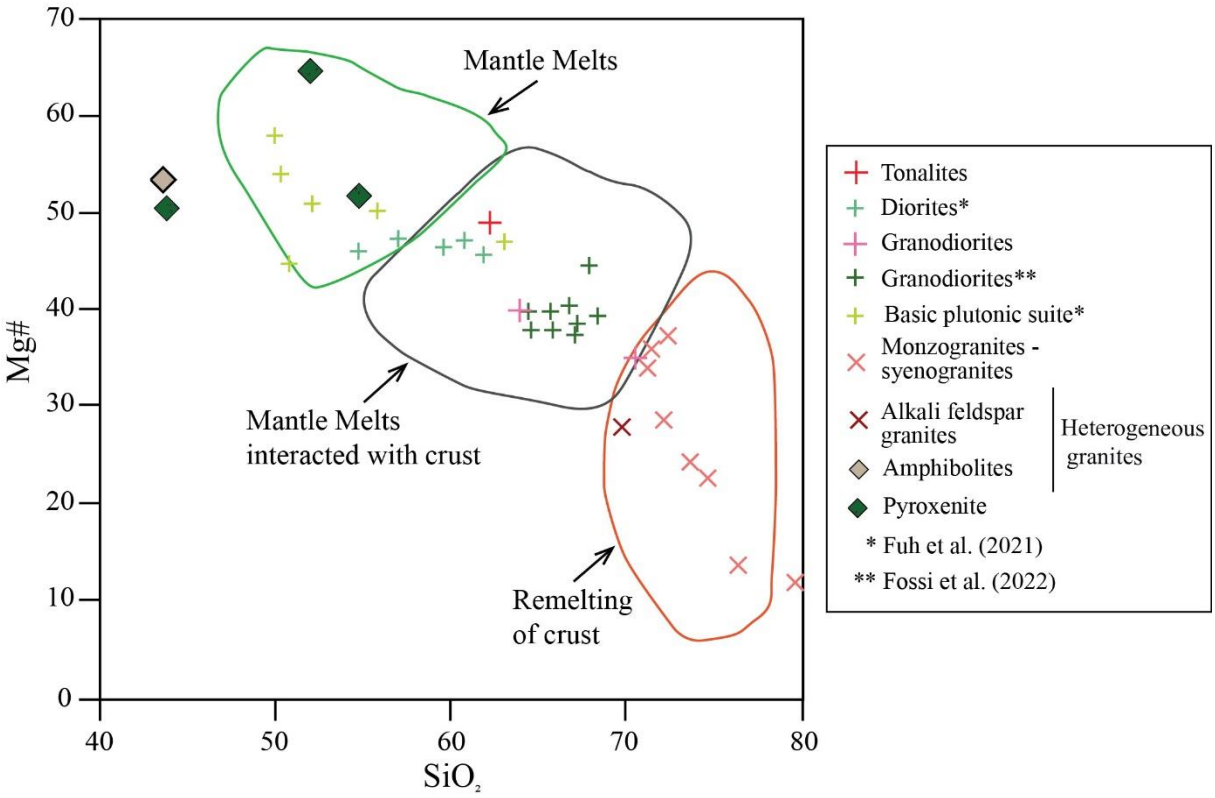

1329

1330 **Figure 15**